

# Simulations of black-hole binaries with unequal masses or nonprecessing spins: Accuracy, physical properties, and comparison with post-Newtonian results

Mark Hannam,<sup>1,2</sup> Sascha Husa,<sup>3</sup> Frank Ohme,<sup>4</sup> Doreen Müller,<sup>5</sup> and Bernd Brügmann<sup>5</sup>

<sup>1</sup>*Faculty of Physics, University of Vienna, Boltzmannngasse 5, A-1090 Vienna, Austria*

<sup>2</sup>*School of Physics and Astronomy, Cardiff University, Cardiff, CF24 3AA, United Kingdom*

<sup>3</sup>*Departament de Física, Universitat de les Illes Balears, Cra. Valldemossa Km. 7.5, Palma de Mallorca, E-07122 Spain*

<sup>4</sup>*Max-Planck-Institut für Gravitationsphysik, Am Mühlenberg 1, 14475 Potsdam, Germany*

<sup>5</sup>*Theoretical Physics Institute, University of Jena, 07743 Jena, Germany*

(Received 12 August 2010; published 3 December 2010)

We present gravitational waveforms for the last orbits and merger of black-hole-binary systems along two branches of the black-hole-binary parameter space: equal-mass binaries with equal nonprecessing spins, and nonspinning unequal-mass binaries. The waveforms are calculated from numerical solutions of Einstein's equations for black-hole binaries that complete between six and ten orbits before merger. Along the equal-mass spinning branch, the spin parameter of each black hole is  $\chi_i = S_i/M_i^2 \in [-0.85, 0.85]$ , and along the unequal-mass branch the mass ratio is  $q = M_2/M_1 \in [1, 4]$ . We discuss the construction of low-eccentricity puncture initial data for these cases, the properties of the final merged black hole, and compare the last 8–10 gravitational-wave cycles up to  $M\omega = 0.1$  with the phase and amplitude predicted by standard post-Newtonian (PN) approximants. As in previous studies, we find that the phase from the 3.5PN TaylorT4 approximant is most accurate for nonspinning binaries. For equal-mass spinning binaries the 3.5PN TaylorT1 approximant (including spin terms up to only 2.5PN order) gives the most robust performance, but it is possible to treat TaylorT4 in such a way that it gives the best accuracy for spins  $\chi_i > -0.75$ . When high-order amplitude corrections are included, the PN amplitude of the ( $\ell = 2$ ,  $m = \pm 2$ ) modes is larger than the numerical relativity amplitude by between 2–4%.

DOI: [10.1103/PhysRevD.82.124008](https://doi.org/10.1103/PhysRevD.82.124008)

PACS numbers: 04.30.Db

## I. INTRODUCTION

One of the most urgent goals of numerical relativity (NR) is to produce simulations that will aid the detection of gravitational waves (GWs) from black-hole-binary mergers. The current first generation of ground-based interferometric GW detectors is about to be upgraded, and the second-generation Advanced LIGO and Virgo detectors are expected to come online around 2014 [1–4]. Once operational, current event-rate calculations predict that they may observe multiple GW signals in one month of design-sensitivity operation [1]. Some of these signals will be from the inspiral and merger of two black holes, and to find them in the detector data GW astronomers will use matched filtering techniques, for which they require large collections of accurate theoretical waveforms (templates) of the physical signal.

The GW signal from the last orbits and merger of black-hole-binary systems can only be calculated in full general relativity using numerical solutions of Einstein's equations. Since such simulations became possible in 2005 [5–7], they have been used to explore larger regions of the black-hole-binary parameter space (which is parametrized by the mass ratio of the binary, the spin vector of each black hole, and the binary's eccentricity), with increasing levels of accuracy and covering increasing

numbers of GW cycles before merger [8,9]. In addition to use in producing analytic waveform models for the construction of GW search template banks, which we will discuss further in this paper, NR waveforms have also been useful in GW detection efforts as part of the NINJA project to test a battery of current GW search pipelines [10,11].

In this paper we present simulations that cover between six and ten binary orbits before merger of configurations in two important subfamilies of the binary parameter space: unequal-mass binaries in which the black holes are not spinning, and equal-mass binaries where the black holes have equal spins either aligned or anti-aligned with the binary's orbital angular momentum.

Following a brief summary of numerical methods in Sec. II, in Sec. III we extend the method we developed in [12] to produce low-eccentricity parameters for spinning binaries. This method is based on integrating the post-Newtonian (PN) equations of motion from a separation where quasicircular (QC) parameters are sufficiently accurate, up to the binary separation where we wish to begin a full numerical simulation, and then using the momenta at that separation from the PN integration as the initial momenta of the full numerical simulation. We now incorporate the highest-order known spin contributions, but find that these are still not accurate enough, and develop a

method to further refine the PN predictions. This allows us to produce simulations of unequal-mass nonspinning and equal-mass spinning binaries with eccentricities of  $e \leq 0.004$ .

In the Samurai study [13] it was shown that current numerical simulations for the equal-mass nonspinning case are well within the accuracy requirements for detection with ground-based experiments. That study also showed that the agreement of numerical results between different codes was consistent with the error estimates of each code—and so a complete error analysis of a set of numerical simulations can confidently be considered as providing the uncertainty in those waveforms with respect to the true physical waveforms. In Sec. V we study the errors in our unequal-mass and equal-mass-spinning waveforms, and conclude that these waveforms are also well within the accuracy requirements for GW detection.

We also estimate the phase accuracy of our simulations, using a number of different methods. The phase error accumulates quickly during the inspiral and even faster during the merger, and small errors at a given separation or frequency are amplified during the further evolution. On the other hand, the absolute value of the GW phase is not directly observable, and phases from different simulations can be aligned in different ways, e.g., between two suitably chosen fixed frequencies during the evolution. Correspondingly, the estimated phase errors show a dramatic dependence on such alignment effects, and it is therefore useful to phrase error estimates in a number of different ways. An example relevant to a comparison with PN results would be the time-domain phase error over a given set of GW cycles, while for GW detection we might be more interested in the mismatch error in the waveform at a given binary mass with respect to a given detector.

Having described the production of our numerical waveforms, and established their accuracy, we summarize in Sec. VI the physical properties of the configurations we have studied: the mass and spin of the final merged black hole, the recoil (in the unequal-mass cases), and the radiated energy and its distribution among the dominant and subdominant harmonics.

One of the motivations for producing black-hole-binary simulations is to use the resulting waveforms for the construction of analytic waveform models. All such models are based in some way on the expectation that PN approximations will be sufficiently accurate up until a few orbits before merger, and so PN (or effective-one-body) results can be used to model the early inspiral, and numerical results can be used to calibrate a model for the merger. Such a procedure first requires a measurement of the accuracy of PN results as the binary approaches merger. We do this in Sec. VII, where we compare the phase and amplitude of our NR results with the corresponding PN predictions over the 8–10 cycles prior to the point where the GW frequency reaches  $M\omega = 0.1$ , about 1.5 orbits

before merger. This extends our previous studies of the equal-mass nonspinning binary [14,15] and equal-mass binaries in the orbital-hang-up configuration [16].

## II. NUMERICAL METHODS

We performed numerical simulations with the BAM code [17,18]. The code starts with black-hole-binary puncture initial data [19,20] generated using a pseudospectral elliptic solver [21], and evolves them with the  $\chi$  variant of the moving-puncture [6,7] version of the Baumgarte-Shapiro-Shibata-Nakamura [22,23] formulation of the  $3+1$  Einstein evolution equations. Spatial finite-difference derivatives are sixth-order accurate in the bulk [18], Kreiss-Oliger dissipation terms converge at fifth order, and a fourth-order Runge-Kutta algorithm is used for time evolution. The gravitational waves emitted by the binary are calculated from the Newman-Penrose scalar  $\Psi_4$ , and the details of our implementation of this procedure are given in [17].

In each simulation, the black-hole punctures are initially a coordinate distance  $D$  apart, and are placed on the  $y$  axis at  $y_1 = -qD/(1+q)$  and  $y_2 = D/(1+q)$ , where  $q = M_2/M_1$  is the ratio of the black-hole masses in the binary, and we always choose  $M_1 < M_2$ . The masses  $M_i$  are estimated from the Arnowitt-Deser-Misner (ADM) mass at each puncture, according to the method described in [19]; we discuss this estimate of the black-hole masses and its subtleties for spinning black holes in more detail in the Appendix. The Bowen-York punctures are given momenta  $p_x = \mp p_t$  tangential to their separation vector, and  $p_y = \pm p_r$  towards each other. The latter momentum component accounts for the (initially small) radial motion of the black holes as they spiral together. One essential question in setting up our simulations is the determination of the parameters  $(p_t, p_r)$  that lead to noneccentric quasicircular inspiral. We will discuss our procedure to generate low-eccentricity parameters in Sec. III.

The grid setup is similar to what we have used in [17], and using the notation introduced there, the simulations discussed in this paper all use a configuration of the form  $\chi_{M\eta=2}[l_1 \times N:l_2 \times 2N:6]$ . This indicates that the simulation used the  $\chi$  variant of the moving-puncture method,  $l_1$  nested mesh-refinement boxes with a base value of  $N^3$  points surround each black hole, and  $l_2$  nested boxes with  $(2N)^3$  points surround the entire system, and there are six mesh-refinement buffer points. The  $\eta$  parameter in the Baumgarte-Shapiro-Shibata-Nakamura system is  $M\eta = 2$ . The choices of  $N$ ,  $l_1$ ,  $l_2$  and the resolutions are given in Table I. The resolution around the puncture is denoted by  $M_1/h_{\min}$ , which is the resolution with respect to the *smallest black hole*,  $M_1$ . The puncture of the second black hole will have the same numerical resolution, but if the black hole is bigger,  $M_2 > M_1$ , then it will effectively be better resolved.

TABLE I. Summary of grid setup for numerical simulations. The grid parameters follow the notation introduced in [17]; see text.  $M_1/h_{\min}$  denotes the resolution on the finest level with respect to the *smallest black hole*, while  $h_{\max}/M$  is the resolution on the coarsest level with respect to the *total mass*,  $M = M_1 + M_2$ . The outer boundary of the computational domain is at  $x_{i,\max}/M$ , where  $x_i = \{x, y, z\}$ . In general  $l_1$  indicates the number of moving refinement levels around each puncture, and  $l_2$  the number of large refinement levels that encompass both punctures. The one exception is the second  $q = 4$  series, which uses three refinement levels around the puncture of the large black hole, and five around the other.

| Configuration            | $N$        | $(l_1, l_2)$ | $M_1/h_{\min}$     | $h_{\max}/M$        | $x_{i,\max}/M$ |
|--------------------------|------------|--------------|--------------------|---------------------|----------------|
| Equal-mass simulations   |            |              |                    |                     |                |
| $\chi_i = -0.85$         | 72, 80, 88 | (6,5)        | 48, 53.3, 58.67    | 10.67, 9.6, 8.73    | 774            |
| $\chi_i = -0.75$         | 80, 88, 96 | (6,5)        | 53.3, 58.67, 64    | 9.6, 8.73, 8.0      | 774            |
| $\chi_i = -0.50$         | 64, 72, 80 | (6,5)        | 42.67, 48, 53.3    | 12.0, 10.67, 9.6    | 774            |
| $\chi_i = -0.25$         | 64, 72, 80 | (6,5)        | 42.67, 48, 53.3    | 12.0, 10.67, 9.6    | 774            |
| $\chi_i = 0$             | 64, 72, 80 | (5,5)        | 21.3, 24, 26.7     | 12.0, 10.67, 9.6    | 774            |
| $\chi_i = 0.25$          | 80, 88, 96 | (5,5)        | 26.7, 29.33, 32    | 9.6, 8.73, 8.0      | 774            |
| $\chi_i = 0.50$          | 80, 88, 96 | (5,5)        | 26.7, 29.33, 32    | 9.6, 8.73, 8.0      | 774            |
| $\chi_i = 0.75$          | 64, 72, 80 | (6,5)        | 42.67, 48, 53.3    | 12.0, 10.67, 9.6    | 774            |
| $\chi_i = 0.85$          | 64, 72, 80 | (6,5)        | 42.67, 48, 53.3    | 12.0, 10.67, 9.6    | 774            |
| Unequal-mass simulations |            |              |                    |                     |                |
| $q = 2$                  | 70, 80, 88 | (5,7)        | 23.3, 26.67, 29.33 | 29.26, 25.6, 23.27  | 2063           |
| $q = 3$                  | 70, 80, 88 | (5,7)        | 23.3, 26.67, 29.33 | 21.94, 19.2, 17.45  | 1547           |
| $q = 4(a)$               | 70, 80, 88 | (5,7)        | 23.3, 26.67, 29.33 | 17.55, 15.36, 13.96 | 1237           |
| $q = 4(b)$               | 80, 88, 96 | (3/5, 7)     | 26.67, 29.33, 32.0 | 15.36, 13.96, 12.8  | 1237           |

The one exception to this setup is a second convergence series for mass ratio  $q = 4$  (see the last row in Table I). These simulations use a grid configuration in which the effective finest resolution is the same for both black holes. This is achieved by putting different numbers of refinement boxes around each puncture. As  $M_1$  is 4 times smaller than  $M_2$ , we use two more boxes (the resolution doubles from box to box) around the smaller black hole than we do for the larger one.

Far from the sources, the meaningful length scale is the total mass of the binary,  $M = M_1 + M_2$ , and so the resolution on the coarsest level is given by  $h_{\max}/M$ .

In our previous study of  $\chi_i > 0$  cases [16] we found that extra resolution was required around the punctures when the black holes have high spin,  $|\chi_i| \gtrsim 0.75$ . In the newer  $\chi_i < 0$  simulations we use high resolution around the puncture in all cases. Note also that in only two cases ( $q = 2, 3$ ), is the outer boundary causally disconnected from the physical system for the entire length of the simulation. This can be seen by comparing the time when the GW signal reaches its peak amplitude in Table IV (to be discussed in Sec. VI), and the location of the outer boundary in Table I.

### III. SPECIFICATION OF LOW-ECCENTRICITY INITIAL PARAMETERS

Puncture initial data typically consist of the analytic Bowen-York solution to the momentum constraint [20] (which allows for the construction of multiple boosted, spinning black holes), and a numerical solution of the Hamiltonian constraint in puncture form [19]. To produce the data for the simulations that we discuss in this paper we

used the single-domain spectral elliptic solver described in [21]. In this approach the black holes' angular and linear momenta may be directly specified, while their masses are specified indirectly. Some subtle issues related to the estimation of black-hole masses are discussed in the Appendix.

We wish to simulate black holes following noneccentric inspiral. Eccentricity cannot be so easily defined in full general relativity as in Newtonian theory, since radiation reaction precludes the existence of circular orbits, and gauge effects mean that any definition based on the coordinate motion of the black holes (or the punctures) will not be unique. Having said that, all definitions of eccentricity based on the gauge-invariant gravitational-wave signal (see [24] for a thorough discussion of the choices available) should agree on zero-eccentricity inspiral, and we have found in previous work [12] that definitions based on the coordinate motion are acceptable at the level of accuracy that we are interested in, which is eccentricities on the order of  $e \sim 10^{-3}$ . For this work we estimate the eccentricity from the orbital frequency of the puncture motion by the maximum of  $e_\omega = (\omega(t) - \omega_c(t))/(2\omega_c(t))$ , where  $\omega_c(t)$  is an estimate of the noneccentric frequency based on a curve fit through the numerical data [12].

To produce low-eccentricity inspiral we need to know the appropriate initial momenta to give the black holes. In puncture simulations the most effective way to do this seems to be to estimate the momenta using PN theory. The simplest approach is to consider only a conservative PN model (i.e., without radiation reaction, and therefore without inspiral), and to calculate the momenta consistent with circular orbits at a given coordinate separation. We will

refer to these as *quasicircular* parameters. We have used QC parameters in the past [17,25,26] for binaries no more than three orbits away from merger, at which point small eccentricities are hard to detect. For binaries that undergo five or more orbits before merger, it becomes clear that the QC momenta result in noticeable eccentricities.

One way to improve the parameters is to use a PN approach that includes the effects of radiation reaction. A straightforward method to do this is by time integration of the PN equations of motion. One begins with QC parameters for a binary with a large separation ( $D \geq 30M$ ), and integrates the PN equations of motion for two point particles until they have reached the separation at which we wish to start a full numerical simulation. At that point we read off the parameters from the PN calculation and use those in our black-hole evolution code. We will refer to such parameters as *PN inspiral (PN)* parameters. In [12] we demonstrated that, in the equal-mass nonspinning case, PN inspiral parameters using a 3PN accurate Hamiltonian [27–29] (see also [30–32]) and 3.5PN accurate radiation flux [33–35] lead to inspirals with eccentricities  $e \sim 0.002$ . Similar results were also obtained for unequal-mass nonspinning binaries up to mass ratio  $q = M_2/M_1 = 4$ ; these were first used in [36], and are discussed in more detail here. PN inspiral parameters were also used successfully to produce low-eccentricity simulations of one precessing-spin configuration in [37].

When we extended our studies to spinning binaries in [16] we found that the same procedure did not work so well. At that time the PN equations included only leading-order (LO) contributions to the spin-orbit and spin-spin Hamiltonians [38–43], and spin-induced radiation flux terms as described in [44], see also [41,43]. Note that there can be ambiguities in the literature assigning PN orders to the spin-terms in the Hamiltonian. Following [45] we assign 1.5PN order to the LO spin-orbit term in the Hamiltonian and 2PN order to the leading-order spin-spin term.

We find that the corresponding LO PN inspiral parameters lead to inspirals with eccentricities  $e \sim 0.009$  for spins parallel to the orbital angular momentum (and  $\chi_i = S_i/M_i^2 = 0.5$ ), and  $e \sim 0.03$  for the corresponding case with spins antiparallel to the orbital angular momentum. In fact, in many cases much lower eccentricities were achieved with the supposedly cruder QC parameters, and these were used for the final results in [16]; in spinning cases the QC parameters include only leading-order spin effects [26,41], and we have not examined the effects of using NLO QC parameters. For the antiparallel-spin cases, both the QC and LO PN inspiral parameters lead to eccentricities that were too high to be seriously considered as “quasicircular inspiral.”

For this work we have incorporated recent results [45–47], and include next-to-leading order (NLO) spin terms in the PN equations of motion. We have also

included the flux contribution due to the energy flowing in to the black holes, which appears at the relative 2.5PN order, as derived in Ref. [48].

The improvement when using NLO PN inspiral parameters is dramatic, as shown in Table. II. We see that in the  $\chi_i = -0.5$  case, the QC parameters lead to an eccentricity of  $e \approx 0.015$ . The LO PN inspiral parameters give even higher eccentricity,  $e \approx 0.03$ . When NLO spin terms are included, however, the eccentricity drops to  $e \approx 0.004$ , i.e., a reduction by almost an order of magnitude.

However, this eccentricity is still twice what we can achieve in the nonspinning case. One approach to reduce further the eccentricity would be to employ an iterative procedure like that used for excision data in [49]. We do not attempt this procedure, for the following reasons. The excision data considered in [49] are adapted to the gauge that will be used for their subsequent evolution, and, in particular, already possess the coordinate motion consistent with their motion along a quasicircular inspiral. Puncture initial data, by contrast, start out with no coordinate motion. After the simulation begins, the puncture *wormholes* evolve into puncture *trumpets* [50–52], and acquire some coordinate motion which, after roughly one orbit, corresponds to the motion consistent with quasicircular inspiral [12]. Measuring the orbital eccentricity in order to apply an iteration procedure therefore requires performing puncture simulations well beyond one orbit, and even then the reduction in eccentricity typically converges very slowly. In addition, it is only really practical to estimate the eccentricity using the puncture coordinate motion, which, as should be clear from the preceding discussion, is purely a gauge effect and so may not be able to be used to reduce the physical eccentricity to an arbitrarily low level. It turns out that a similar effect occurs with excision data, as recently reported in [24]. Note, however, that the results in [24] arise from a different gauge condition to that used in moving-puncture simulations, and any conclusions they draw about the correspondence (or lack thereof) between the coordinate and physical motions of the black holes may not apply to

TABLE II. Choices of the initial momenta and resulting eccentricity for the equal-mass  $\chi_i = -0.5$  case. We find that the QC parameters yield an eccentricity an order of magnitude larger than we desire, while the LO PN inspiral parameters are twice as bad. Incorporating NLO spin effects dramatically reduces the eccentricity to  $e \sim 0.004$ , and a further iteration based on PN predictions reduces it by a further 25%.

| Parameters      | $p_x$    | $p_y (\times 10^{-4})$ | $e$   |
|-----------------|----------|------------------------|-------|
| QC              | 0.084 69 | 0                      | 0.015 |
| PN (LO)         | 0.086 12 | −5.824                 | 0.03  |
| PN (NLO)        | 0.085 00 | −5.250                 | 0.004 |
| PN <sub>+</sub> | 0.085 12 | −5.258                 | 0.003 |
| PN <sub>−</sub> | 0.084 87 | −5.242                 | 0.008 |



moving-puncture results. We will consider this further in future work [53].

For these reasons, we have attempted an alternative approach, based on extracting further information from PN theory. We will illustrate our approach using the same case that we have discussed above. Here the black-hole spins are  $|\chi_i| = 0.5$  and directed antiparallel to the binary's orbital angular momentum. The initial coordinate separation of the punctures is  $D = 12.5M$ . A first simulation is performed using NLO PN inspiral parameters. For reference, these are, as given in Table II,  $p_t/M = 0.0850$  for the tangential momenta, and  $p_r/M = -5.250 \times 10^{-4}$  for the radial momenta.

We then calculate the eccentricity of the first orbits in this simulation. As we stated above, we find  $e \approx 0.004$ . To reduce the eccentricity further, we now return to PN theory. If we solve the PN equations of motion starting at  $D = 12.5M$ , using  $(p_r, p_t)/M = (0.085, -5.25 \times 10^{-4})$ , we will of course recover the same noneccentric PN inspiral as when we first calculated these parameters. We now ask the question, "How much would these parameters have to vary, in order to produce the eccentricity we saw in our NR simulation?" We assume that a variation in  $(p_r, p_t)$  that produces an eccentricity of  $e = 0.004$  in the PN integration, starting at the same separation as the NR simulation, will give us approximately the correct magnitude of momenta variation to remove the eccentricity in the NR simulation. Common simplifying characteristics of the situations we have in mind are that the variation in separation due to eccentricity, during half an orbit, say, is smaller than the variation due to the inspiral; and that the tangential momentum is much larger than the radial momentum.

What we do now is simply adjust both the radial and tangential momenta by some factor  $k$  until the PN evolution produces an eccentricity of  $e \approx 0.004$ . For this case we find that  $k \approx 1.0015$ , i.e., by 0.15%. We then assume that this is close to the error in the parameters that we have used in our NR simulation, and modify those also by 0.15%. We perform two additional simulations, one in which the momenta are increased by 0.15%, and one in which the momenta are reduced by 0.15%. The two enhanced PN-parameter choices are denoted by "PN $_{\pm}$ " in Table II.

We find, in this case, that the eccentricity is reduced when the momenta were reduced, and we achieve  $e \approx 0.003$ . This is very close to the eccentricity we achieved in the equal-mass nonspinning case, and we consider that acceptable. We also experimented with repeating this iteration procedure, but it did not noticeably reduce the eccentricity; at this level it may be possible to more cleverly modify separately the radial and tangential momenta, but it may also turn out that further refinement in the *puncture-motion* eccentricity will not improve the true physical eccentricity, as indicated by the GW signal. At

some level of accuracy it will also be necessary to adjust the radial and tangential momenta by different factors. Another shortcoming of the method we have used here is that we do not explicitly use phasing information when adjusting the eccentricity of the orbit, e.g., to determine whether momenta should be increased or decreased without having to perform two further simulations. One reason why this is difficult, is because in the initial gauge of the simulation the punctures are stationary on the numerical grid, and it takes  $\sim$  one orbit for their motion to asymptote to a trajectory consistent with the physical motion of the black holes. We have found the results to be acceptable for all cases we have considered here. Further work on improving this procedure is underway, and preliminary results on an improved method that also uses phasing information have been presented recently [54].

The procedure we have described here was performed on all of the anti-hang-up cases, and the final parameters are given in Table IV. For these cases we also indicate the eccentricities that were achieved from the raw PN-inspiral parameters. Also shown are the parameters for the nonspinning case presented in [14], the hang-up cases described in [16], and a set of nonspinning unequal-mass simulations. In the unequal-mass simulations, the eccentricity was found to be sufficiently low with the raw PN inspiral parameters, and no further modifications were made. This also suggests that while we expect the PN approximation to deteriorate for larger mass ratios, this deterioration is not large at  $q = 4$ .

However, a second series of  $q = 4$  simulations was also performed, using effective-one-body (EOB) parameters as described in [55]. Whereas PN inspiral parameters lead to an eccentricity of  $e \approx 0.0038$ , the EOB parameters lead to a lower eccentricity of only  $e \approx 0.003$ . This appears to be consistent with the expectation that EOB methods retain their accuracy at higher mass ratios better than PN methods, although we note that the uncertainty in the eccentricity calculation is  $5 \times 10^{-4}$ , and so the two values agree within uncertainty. Results from much higher-mass-ratio simulations are necessary to definitively compare the performance of EOB and PN parameters.

#### IV. SUMMARY OF NUMERICAL SIMULATIONS

In this section we summarize the two sets of configurations that we studied.

The first comprised equal-mass ( $q = 1$ ) binaries, with equal spins directed either parallel ( $\chi_i > 0$ ) or antiparallel ( $\chi_i < 0$ ) to the orbital angular momentum of the binary. The spins considered were  $|\chi_i| = \{0, 0.25, 0.5, 0.75, 0.85\}$ . When the spins are (anti-)parallel to the orbital angular momentum, they will not precess, making such cases a relatively simple subfamily of the total black-hole-binary parameter space. And when  $q = 1$ , the system possesses enough symmetry that the simulation can be performed on only a quarter of the full physical domain,  $z > 0, y > 0$ ; this

symmetry is also reflected in the fact that in these configurations the center of mass of the system does not move, and the final black hole does not experience any recoil.

In addition, the choice of equal spins also yields an important subfamily of configurations: we found in [56] that it is possible to rather accurately model any nonprecessing binaries with *unequal spins* using essentially only a *mass-weighted sum of the spins* of the binary, motivated by numerical evidence from [26,57,58], and PN theory [59]. Therefore for the purposes of producing waveform models for GW detection with current ground-based detectors, it is sufficient to simulate only binaries where the black holes have equal spins. Recall also that the use of Bowen-York-puncture data limits us to black holes with spins  $|\chi_i| \lesssim 0.92$  [60–63], and that since errors due to the presence of junk radiation increase with higher spins, the maximum spin that we treat in these simulations is  $|\chi_i| = 0.85$ .

The second set of configurations we consider is nonspinning binaries with unequal masses,  $q = \{2, 3, 4\}$ . Now the symmetry of the system is reduced, and the simulations require half of the physical domain,  $z > 0$ . The center of mass of the system can move, and does due to the nature of the asymmetry of the GW emission from these systems, and the final black hole “recoils” (or is “kicked”) relative to the original center of mass of the binary. We will discuss further the recoil in our unequal-mass simulations in Sec. VID.

Of the simulations discussed in this paper, a small subset were first presented elsewhere. The equal-mass nonspinning simulations were described in detail in [14], and the  $|\chi_i| > 0$  cases in [16]. The remaining simulations have not yet been published, although they have all been used as part of other studies. The  $q = 2$  simulations were used to study parameter-estimation accuracy for the Laser Interferometric Space Antenna [64]. In addition, all of these simulations have been used to build phenomenological waveform families. Some of the nonspinning-binary data were used in [36,65] to produce nonspinning phenomenological waveforms, and in [66] to calibrate an EOB model. It should be noted, however, that in those works less-accurate simulations of the higher-mass-ratio cases were used, and, in particular, the accuracy of the  $q = 4$  data used in [66] were not sufficiently accurate to conclusively test the physical fidelity of the EOB model. Also, all of the waveforms presented here were used to produce the first non-precessing-spin phenomenological model presented in [56], and the follow-up study in [67]. In fact, extra simulations for unequal-mass *spinning* binaries were also necessary for that work, but we will not consider those here.

The methods we used to estimate the initial momenta for quasicircular inspiral were described in Sec. III, and fall into three classes: quasicircular, PN inspiral (including NLO spin terms when necessary), and enhanced PN $_{\pm}$  inspiral, as described in Sec. III. For an extra  $q = 4$  series, we also used parameters based on an EOB model.

QC parameters were used to produce the older orbital hang-up  $\chi_i > 0$  simulations, which were originally presented in [16]; for these cases the eccentricity is the highest, around  $e \sim 0.006$ . PN inspiral parameters were used for the unequal-mass simulations, where they were found to yield acceptably low eccentricities of  $e < 0.004$ . Finally, PN $_{\pm}$ -inspiral parameters were used for the anti-hang-up cases  $\chi_i < 0$ , and for all cases the eccentricity is  $e < 0.003$ . The EOB parameters that were used for the second  $q = 4$  series lead to an eccentricity of  $e \approx 0.003$ .

## V. ACCURACY OF NUMERICAL SIMULATIONS

In this section we will estimate the errors in our numerical results. These will give us some indication of both the physical accuracy of our waveforms, and the applications for which they can confidently be used.

The waveform can be decomposed into phase and amplitude functions,  $\phi_{\ell m}(t)$  and  $A_{\ell m}(t)$  respectively, for each spherical harmonic mode  $(\ell, m)$ . The individual harmonics of the Newman-Penrose scalar  $\Psi_4$  can now be written as

$$R_{\text{ex}} \Psi_{4,\ell m}(t) = A_{\ell m}(t) e^{-i\phi_{\ell m}(t)}, \quad (1)$$

where  $R_{\text{ex}}$  is the coordinate radius of the wave-extraction sphere. The frequency of the signal is given by  $\omega_{\ell m} = d\phi_{\ell m}/dt$ . The results in this paper use GW signals extracted at  $R_{\text{ex}} = 90M$ , unless otherwise stated.

We will focus on the  $(\ell = 2, m = 2)$  mode. The numerical error in the functions  $A_{22}(t)$  and  $\phi_{22}(t)$  is estimated by means of a convergence test: we perform simulations at three (or more) numerical resolutions, and verify that differences between successive resolutions decrease at a rate consistent with the expected convergence properties of the numerical code. Throughout the remainder of this paper, the functions  $A(t)$ ,  $\phi(t)$  and  $\omega(t)$  will refer to the  $(\ell = 2, m = 2)$  quantities unless otherwise stated. If a clear convergence rate is observed, then it is also possible to use Richardson extrapolation to remove the error term at the next order, and produce a yet more accurate estimate of the true result, and to also calculate an uncertainty estimate. This procedure was carried out for our equal-mass nonspinning data in [14].

As described in Sec. II, we have based our grid configurations on that used in our work on equal-mass nonspinning binaries [14]. For that configuration, the defining number of points in the three convergence series simulations (see Table I) was  $N = \{64, 72, 80\}$ . This was sufficient to achieve reasonably clean sixth-order convergence, which had been identified in [18] as the dominant order of finite-difference error in our code. For configurations with higher mass ratios and nonzero spins, greater numerical resolution is required. In many of the new simulations the number of grid-points has therefore been increased. In some cases the extra resolution was sufficient to again achieve sixth-order convergence, but in others it was not. For these latter cases, although we can be confident that

the simulations are converging towards the continuum solution, we are unable to use Richardson extrapolation to estimate the uncertainties, and must provide much more conservative error estimates. Although we could perform more simulations at yet higher resolution, we find that even these conservative error estimates are within the error bounds required for this work and many GW-astronomy applications.

We will illustrate these points with two representative cases: one that shows clean sixth-order convergence, and one that does not. We focus first on the GW phase, because it is the phase error that dominates the mismatch calculations that are at the heart of the matched-filtering technique used in GW searches, and because the error in the *amplitude* is dominated not by numerical resolution but by the radius  $R_{\text{ex}}$  of the GW extraction; we will discuss this further in Sec. VC.

### A. GW phase

In studying the GW phase, we have two aims: (1) to show that our results are converging to the continuum solution as a function of numerical resolution, and to provide error bounds on the GW phase, and (2) to illustrate the ambiguities inherent in estimating the phase error. The ambiguity in estimating phase errors is already well known, but we discuss it further here to make the point that although the accuracy of the GW phase is important, any one method of estimating the “phase error” may tell us little about the waveform’s accuracy for a given application.

We consider three measures of the phase error. The first is the total accumulated phase error over the length of the simulation. This is the most natural quantity to study in a convergence test. The second is the accumulated phase error over the ten cycles up to a GW frequency of  $M\omega = 0.1$ . We will need this error estimate to justify the comparison with PN results in Sec. VII, but we will also see that this quantity is problematic when used for a convergence test, as is any realignment of the GW phase. None of these estimates have a natural interpretation for applications in GW searches. There the mismatch error is the appropriate measure of the waveform’s accuracy, and we will consider this in Sec. VC.

For our convergence analysis we consider in detail two cases, ( $q = 1, \chi_i = 0.5$ ) and the second ( $q = 4, \chi_i = 0$ ) convergence series. These are indicative of the general features of all of the cases we have studied.

Standard convergence plots of the GW phase are shown in Fig. 1. The initial phases agree at  $t = 0$ , and the plot shows the subsequent evolution of the phase disagreement between simulations at different resolutions. In the  $\chi_i = 0.5$  case (left panel), which uses relatively high resolution for a moderate spin value, we see reasonably clean sixth-order convergence. The  $q = 4$  case, however, even though the numerical resolutions are the same, is not yet in the sixth-order convergence regime, and for these choices of

grid resolutions, appears to be second-order convergent. We emphasize that this is *not* a demonstration that the simulations have entered a second-order convergence regime; while it is expected that at sufficiently high resolutions the second-order accurate components of the code will dominate, we have not yet performed *any* simulations of any configuration with high enough resolution to see clean asymptotic second-order convergence. All the second panel of Fig. 1 tells us is that we are not yet in the fully convergent regime, but since the results are converging, in the sense that the errors reduce between simulations, we can still make a conservative estimate of the accumulated phase error.

In the  $\chi_i = 0.5$  case, we can use Richardson extrapolation based on sixth-order convergence, to estimate the uncertainty in the accumulated phase as 0.6 rad. In the  $q = 4$  case, however, we do not yet see sixth-order convergence. If we were to optimistically assume that the medium- and high-resolution simulations *are* in the convergent regime, and it is only the low-resolution simulation that is not, then we would estimate an accumulated phase uncertainty of 1.9 rad based on Richardson extrapolation. If we instead produce a much more conservative error estimate based on second-order Richardson extrapolation, we find 6.7 rad. Note that this is an order of magnitude higher than we found in the cleaner  $\chi_i = 0.5$  case, and corresponds to a full GW cycle.

How are we to interpret these accumulated phase errors? They are certainly useful in comparing simulations—for example, the second  $q = 4$  convergence series is less accurate than the  $\chi_i = 0.5$  series. But this measure of the phase accuracy is of little additional value. In a GW application we will use only the waveform *after* the passage of the pulse of junk radiation. It is then difficult to estimate the phase error of the resulting waveform because to do so we must first align the waveform at some point after the beginning of the simulation. This introduces ambiguities (due to numerical noise in the GW phase and frequency) that may be larger than the error we ultimately want to measure; this point is illustrated well in Sec. V.E.2 of [68].

When we compare with PN approximants in Sec. VII, we will be interested in the phase error over the 8–10 GW cycles up to GW frequency  $M\omega_m = 0.1$ . If we look at Fig. 1, we find that the accumulated phase difference at that frequency, between the medium- and high-resolution simulations, is 0.1 rad and 0.12 rad, respectively, for the  $\chi_i = 0.5$  and  $q = 4$  cases. However, if we instead line up the waveforms in each convergence series at  $M\omega_m = 0.1$ , and measure the accumulated phase disagreement as we go back 10 cycles, we instead find about 0.01 rad for both configurations. This is an order of magnitude lower than what we observe when the waveforms are aligned at the beginning. This is an artifact of both the removal of the junk-radiation portion of the waveform, and simply the properties of the waveform frequency functions; similar effects are seen with different choices of alignment of PN



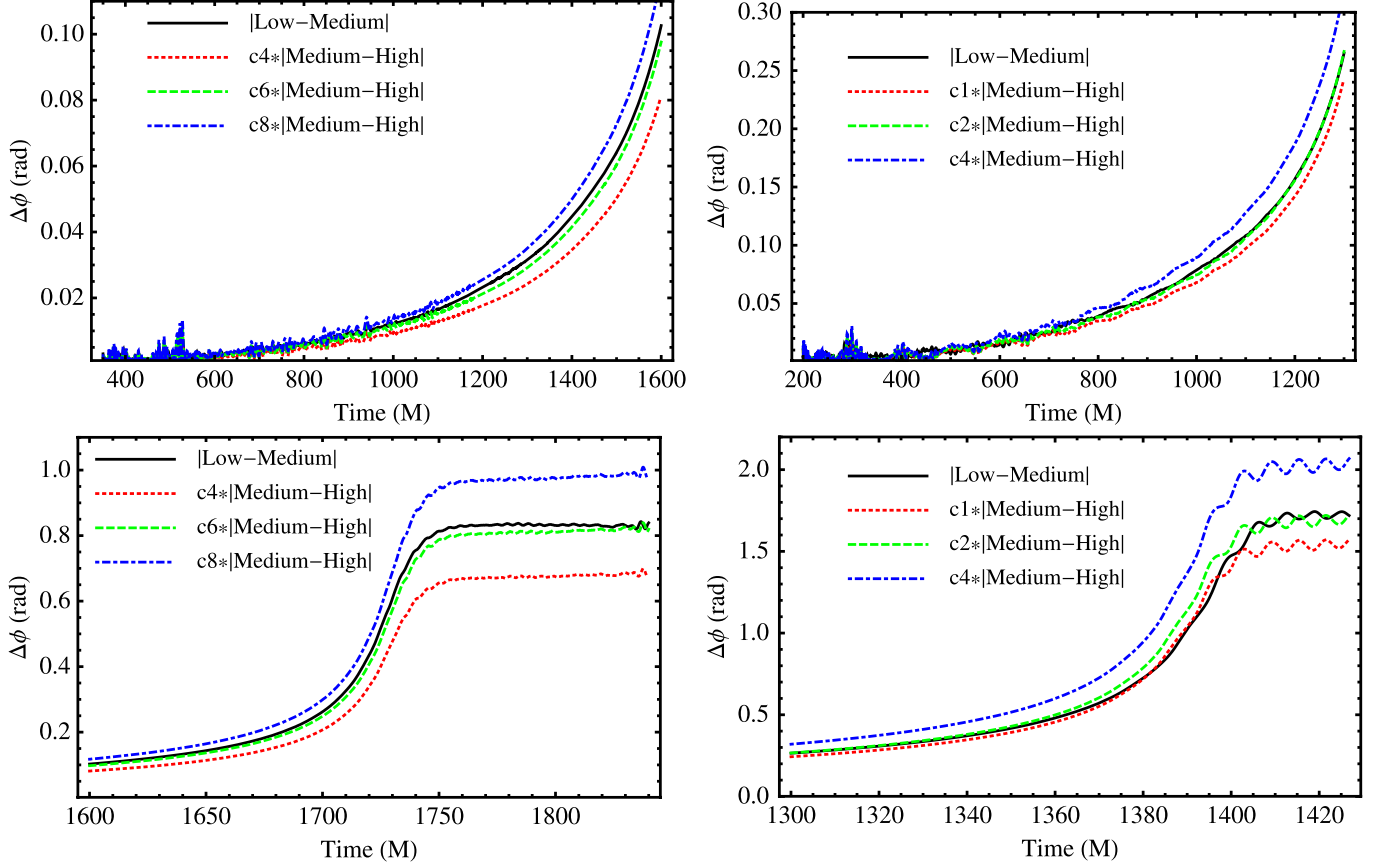


FIG. 1 (color online). Convergence of the phase as a function of time for the  $\chi_i = 0.5$  (left) and  $q = 4$  (second convergence series) cases. The early-time behavior is shown in the upper plots, and the late-time behavior in the lower plots. Scaling with respect to different convergence orders is shown, to illustrate how cleanly the data exhibit a particular convergence behavior. In these plots  $t = 0$  indicates the beginning of the simulation, and  $\Delta\phi(t = 0) = 0$  in all simulations. The  $\chi_i = 0.5$  case shows reasonably clean sixth-order convergence, and the accumulated phase difference is  $\Delta\phi = 0.43$  rad between the medium- and high-resolution simulations. The  $q = 4$  case is not yet in the sixth-order convergent regime, and appears (erroneously) to exhibit second-order convergence. The accumulated phase difference between the medium- and high-resolution simulations is 1.5 rad.

waveforms, for which no junk radiation or significant numerical noise exist.

These results demonstrate that we must be careful to choose our assessment of the phase error consistently with the application we are interested in. For the PN phase comparison in Sec. VII, we compare PN and NR waveforms aligned at  $M\omega_m = 0.1$ , and so the only meaningful numerical phase error estimate that makes sense is that based on the same form of phase alignment.

Noise in the numerical frequency introduces an ambiguity into the matching time for any phase re-alignment procedure, which makes it impossible to use the realigned phase as the basis of a convergence test. However, we can vary the matching time within its error bounds, measure the *maximum* accumulated phase disagreement that arises from this process, and then use fourth-order Richardson extrapolation to provide a conservative error estimate in the phase. The results of this process are shown in Table III, and will be relevant to the analysis in Sec. VII. The same procedure and alignment are used to give estimates of the

phase uncertainty accumulated during merger and ring-down. The table also shows an estimate of the total accumulated phase error, based on a convergence analysis like that shown in Fig. 1; we repeat that this estimate has no direct relation to any physical application, and is only useful as a means to compare the relative accuracy of different simulations. Note that this number is *not* simply the sum of the inspiral and merger phase uncertainty estimates, and this is a clear artifact of the alignment ambiguity in assessing phase accuracy. As such, in most physical applications, where some realignment is implicitly performed, the effective total phase error may drop by an order of magnitude over the numbers shown in the table. It is also clear that the total accumulated phase error estimates depend dramatically on whether we see clean convergence (the one truly clean case shown in the table is  $\chi_i = 0.5$ ; other lower spin cases are also cleanly convergent). Nonetheless, we will see in Sec. V C that this level of accuracy is still well within the requirements for GW detection.



TABLE III. Estimates of uncertainty in phase and amplitude. The phase uncertainty accumulated during the inspiral is based on an alignment of the GW phase at  $M\omega = 0.1$ , and includes only the ten GW cycles up to that frequency, for consistency with the analysis in Sec. VII. The same alignment is used for the phase uncertainty of the merger and ringdown regime. The complete phase uncertainty is a conservative estimate of the total accumulated phase error over the entire waveform, and is *only* relevant for relative comparisons of different simulations; see text in Sec. VA. The amplitude uncertainties are described in Sec. VB, and the mismatch errors in Sec. VC.

| Case             | Phase uncertainty (radians) |        |          | Amplitude uncertainty (percentage) |        | Mismatch ( $\times 10^{-4}$ ) |
|------------------|-----------------------------|--------|----------|------------------------------------|--------|-------------------------------|
|                  | Inspiral                    | Merger | Complete | Inspiral                           | Merger |                               |
| $q = 1$          |                             |        |          |                                    |        |                               |
| $\chi_i = +0.85$ | 0.1                         | 2.10   | 10       | 0.25                               | 5.0    | 2.8                           |
| $\chi_i = +0.50$ | 0.05                        | 0.75   | 1.0      | 0.5                                | 1.0    | 1.0                           |
| $\chi_i = -0.50$ | 0.1                         | 0.80   | 10       | 0.5                                | 4.0    | 0.8                           |
| $\chi_i = -0.85$ | 0.1                         | 0.75   | 15       | 0.5                                | 2.0    | 0.7                           |
| $q = 2$          | 0.05                        | 0.2    | 5.0      | 0.2                                | 1.0    | 0.3                           |
| $q = 3$          | 0.05                        | 0.3    | 10       | 0.4                                | 2.0    | 2.7                           |
| $q = 4(a)$       | 0.1                         | 1.5    | 15       | 0.25                               | 4.0    | 3.2                           |
| $q = 4(b)$       | 0.05                        | 0.8    | 7.0      | 0.25                               | 2.0    | ...                           |

### B. GW amplitude

We now consider the GW amplitude. This plays a less important role in *detection*, but errors in the amplitude (as well as higher harmonics) will affect estimates of the source parameters, since all parameter errors scale with inverse signal-to-noise ratio.

If we perform a time-domain convergence analysis of the GW amplitude, our conclusions are biased because the apparent amplitude error is in fact a combination of both the amplitude *and* phase errors—if the amplitude were measured with no error by the code, but two waveforms are out of phase, they will appear to have a nonzero amplitude error when compared in the time domain. We discussed this point in some detail in [14], and used a parametrization of the amplitude in terms of GW phase to reduce the effects of dephasing on the amplitude analysis. This works well if the phase error as a function of GW frequency is small, but this will not always be true. We expect (from the PN and perturbation theories) that the GW amplitude is a function of the GW frequency, and so the ideal method to measure the amplitude accuracy would be to reparametrize the amplitude as a function of GW frequency.

This procedure also presents problems: the GW frequency is a numerically noisy function during the early

and late parts of the simulation; it is certainly not the smooth monotonically increasing function that we expect it to be on physical grounds. We can partially circumvent this difficulty by producing a smooth analytic fit of the frequency function, and considering the GW phase and amplitude as parametrized by that function. The smoothing process may itself introduce numerical artifacts, and either mask or exaggerate the convergence properties of the numerical results. But in general it is sufficient to allow us to calculate uncertainty estimates for our waveforms.

Our method for modeling the GW frequency is as follows, based on an earlier version that was used (for equal-mass, nonspinning waveforms) in the work for the Samurai project [13]. For the inspiral, we start with the analytic TaylorT3 approximant for the frequency, as given in [69]. We neglect the highest-order (3.5PN) nonspinning term and replace it by a free parameter that will be fit to our data. In addition, following [69], we do not specify the value of the spin, but also treat it as a free parameter—remember that our goal is to produce a clean analytic fit to the frequency, and we are not interested in whether all of the parameters have their usual physical interpretation. The modified TaylorT3 frequency function is then

$$\begin{aligned}
\Omega_{\text{PN}}(\tau) = & \frac{1}{4} \tau^{-3/8} \left[ 1 + \left( \frac{743}{2688} + \frac{11}{32} \nu \right) \tau^{-1/4} - \frac{3}{10} \pi \tau^{-3/8} + \left( \frac{47}{40} \frac{S}{M^2} + \frac{15}{32} \frac{\delta M}{M} \frac{\Sigma}{M^2} \right) \tau^{-3/8} \right. \\
& + \left( \frac{1855099}{14450688} + \frac{56975}{258048} \nu + \frac{371}{2048} \nu^2 \right) \tau^{-1/2} + \left( -\frac{7729}{21504} + \frac{13}{256} \nu \right) \pi \tau^{-5/8} + \left[ \left( \frac{101653}{32256} + \frac{733}{896} \nu \right) \frac{S}{M^2} \right. \\
& + \left. \left( \frac{7453}{7168} + \frac{347}{896} \nu \right) \frac{\delta M}{M} \frac{\Sigma}{M^2} \right] \tau^{-5/8} + \left( -\frac{720817631400877}{288412611379200} + \frac{53}{200} \pi^2 + \frac{107}{280} \gamma - \frac{107}{2240} \ln\left(\frac{\tau}{256}\right) \right. \\
& \left. \left. + \left( \frac{25302017977}{4161798144} - \frac{451}{2048} \pi^2 \right) \nu - \frac{30913}{1835008} \nu^2 + \frac{235925}{1769472} \nu^3 \right) \tau^{-3/4} + a \tau^{-7/8} \right],
\end{aligned}$$

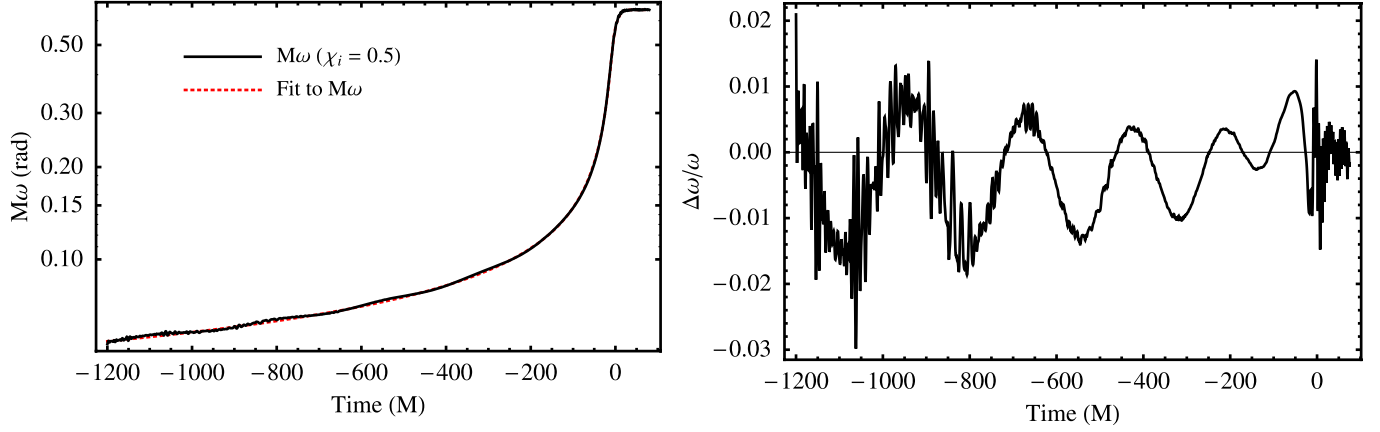


FIG. 2 (color online). Analytic fit to the GW frequency for the  $\chi_i = 0.5$  case. The right panel shows the fractional difference between the fit and numerical data. For this configuration, the error in the fit is dominated by the residual eccentricity in the simulation. The dashed line indicates the point at which the amplitude reaches its maximum.

where  $\nu = m_1 m_2 / M^2$  is the symmetric mass ratio,  $S = S_1 + S_2$  is the total spin parallel to the orbital angular momentum,  $\Sigma = M(S_2/m_2 - S_1/m_1)$ , and  $\delta M = m_1 - m_2$ . (Note that in the Samurai paper, the PN frequency formula Eq. (7) is missing an overall factor of 2.) In the cases we consider here, the spins are nonzero only in the equal-mass case, and the spins are always equal to each other, so the  $(\delta M \Sigma)$  terms do not contribute. The function  $\tau$  is usually given by  $\tau = \nu(t_c - t)/(5M)$ , and  $t_c$  is interpreted as the “time of coalescence” in standard PN theory, although a more appropriate term would be “time of divergence”.

In order to produce a formula that can be fit through our data, we redefine  $\tau$  as

$$\tau^2 = \frac{\nu^2(t_c - t)^2}{25M^2} + d^2, \quad (2)$$

where both  $t_c$  and  $d$  are free parameters that are fit to the data. This modification of  $\tau$  prevents  $\Omega_{\text{PN}}$  from diverging at  $t = t_c$ . In the form that we have written it,  $\Omega_{\text{PN}}$  is now symmetric about  $t = t_c$ , which is certainly not physically realistic, but beyond this point we will make a smooth transition to a different function, which models the ringdown.

To model the ringdown phase, we modify the ansatz suggested in [70], and write the full frequency as

$$\Omega(t) = \Omega_{\text{PN}}(\tau) + [\Omega_f - \Omega_{\text{PN}}(\tau)] \times \left( \frac{1 + \tanh[\ln \sqrt{\kappa} - (t - t_0)/b]}{2} \right)^\kappa. \quad (3)$$

The constants  $\{t_c, t_0, S, \kappa, a, b, \Omega_f\}$  are parameters that are determined to produce the best fit to the numerical data. The constant  $\Omega_f$  corresponds to a fit of the ringdown frequency, but the other parameters have no clear physical interpretation. (Even the “spin” parameter  $S$  really

amounts to no more than a modification of the 1.5PN and 2.5PN terms in the description of the inspiral frequency.)

Figure 2 shows a typical frequency fit, in this case for  $\chi_i = 0.5$ . We see that the dominant error in the fit is due to the residual eccentricity in this simulation; recall that the aligned-spin cases are based on QC parameters and have the highest eccentricity of all the cases we studied. The procedure does not work quite so well in cases with high spin; the frequency evolution is not captured so well during the early inspiral, or in the 200M before the peak GW amplitude. The fitting formula (2) could be modified to address this, and indeed the model of the transition to ringdown (3) has since been improved by the authors of [70,71]. These issues, and the masking of eccentricity effects, mean that this frequency fit is far from ideal, and cannot be used for a convergence study of the amplitude. However, it is adequate for the purpose of providing a rough estimate of the amplitude uncertainty in our simulations.

Figure 3 shows the differences in  $A(\omega)$  with respect to resolution for the  $\chi_i = 0.5$  configuration. The figure suggests that the error in the GW amplitude due to numerical resolution is on the order of 1%. At late times the relative error grows higher, but this is beyond the frequency at which the amplitude reaches a maximum (indicated by the dashed line), and is well into the ringdown of the signal. Note that if we perform an error analysis based on the time-domain amplitude, then the maximum error between the medium- and high-resolution simulations is around 6%, which suggests that it is indeed dominated by the phase error.

Estimates for the amplitude uncertainty (using the amplitude parametrized by GW frequency) are given in Table III. In all cases the GW signal was extracted at  $R_{\text{ex}} = 90M$ ; we will discuss the errors due to the use of a finite extraction radius in the next section.

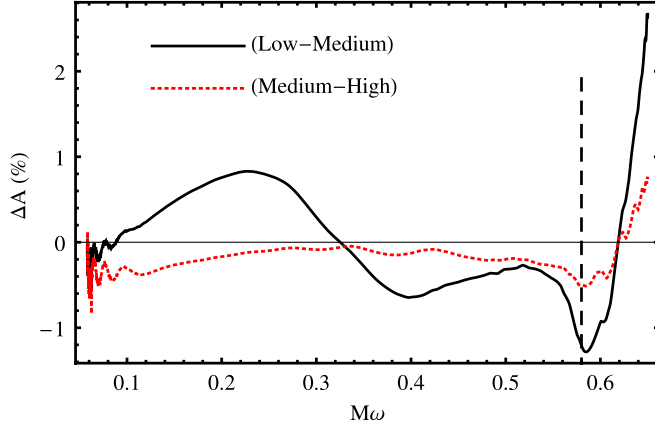


FIG. 3 (color online). The amplitude error as a function of GW frequency for the  $\chi_i = 0.5$  case. The deficiencies of the frequency fitting procedure preclude the use of  $A(\omega)$  for a convergence test, and the differences between the low-, medium-, and high-resolution simulations are not scaled in any way.

### C. Mismatch with respect to numerical frequency and GW extraction radii

Ultimately we are interested in the accuracy of our waveforms with respect to GW detection. The most meaningful way to do this is to calculate the *faithfulness* between waveforms from different numerical resolutions and different extraction radii.

A calculation of the faithfulness is based on the overlap between two waveforms. The overlap is usually calculated in the frequency domain. For two GW signals (in this analysis all quantities are with respect to the  $(\ell = 2, m = 2)$  mode of the signal)  $\tilde{h}_1(f)$  and  $\tilde{h}_2(f)$ , we define an inner product weighted by the power spectral density of the detector noise,  $S_n(f)$ , as [72],

$$\langle h_1 | h_2 \rangle := 4\text{Re} \left[ \int_{f_{\min}}^{f_{\max}} \frac{\tilde{h}_1(f) \tilde{h}_2^*(f)}{S_n(f)} df \right]. \quad (4)$$

Our data represent  $\Psi_4(t)$ , not the wave strain  $h(t)$ , but the two are related by  $\Psi_4 = \ddot{h}_+ - i\ddot{h}_\times$ . Making two time integrations is trivial when transforming to the frequency domain, and although this does not automatically remove the irritation of having to choose constants of integration (see [73] for a recent discussion of this problem) we have found that our ignorance of these constants does not affect mismatch calculations [13].

Given the definition of the inner product  $\langle h_1 | h_2 \rangle$ , we normalize it and maximize over phase and time offsets in the data. If the waveforms were equal, then this quantity would be unity. This is the faithfulness of the waveform: it is a measure of how “far” a theoretical waveform is from a supposedly true waveform with the same physical parameters. We define the *faithfulness mismatch* as the deviation from unity:

$$\mathcal{M} = 1 - \max_{\tau, \Phi} \frac{\langle h_1 | h_2 \rangle}{\sqrt{\langle h_1 | h_1 \rangle \langle h_2 | h_2 \rangle}}. \quad (5)$$

Ideally the integrations over frequency are in the range  $[0, \infty]$ . When we have a finite data set like our numerical waveforms, we also need to optimize with respect to the window of our data that we sample. This is discussed in further detail in [13]; the optimization with respect to phase and time offset is trivial in the frequency domain when using only one the  $(\ell = 2, m = 2)$  mode. In general more sophisticated maximization procedures are required, for example, the techniques described in [74] for the quadrupole harmonic, and in [75] for signals that include higher harmonics.

The faithfulness mismatch is calculated without any optimization over the intrinsic parameters of the binary. In a true GW search using a bank of theoretical templates, one optimizes not only over time and phase shifts, but over all physical parameters included in the template bank. Optimization over the physical (intrinsic) parameters gives the *effectualness mismatch*, i.e., how well a waveform family will be able to detect GW signals irrespective of whether the physical parameters are measured correctly. We have access to waveforms representing only one choice of intrinsic parameters of the binary, and so cannot perform this optimization (although we could easily optimize over the total mass of the binary). The physical-parameter-optimized effectualness mismatch will always be better than (or equal to) the faithfulness mismatch and so we can use the faithfulness to set an upper bound on the error of the waveforms.

The faithfulness mismatch between the simulations of different resolutions is negligible—it is below  $10^{-6}$  for all relevant masses (down to about  $100M_\odot$ ) with respect to the Advanced LIGO noise curve [76] (we use the approximate analytical formula displayed in [36]), where we choose a low-frequency cutoff of 20 Hz.

We also use the faithfulness to estimate the error due to the finite extraction radii. The GW signal is extracted on spheres of radii  $R_{\text{ex}} = \{50, 60, 70, 80, 90\}M$ , and we expect the error relative to the true signal as  $R_{\text{ex}} \rightarrow \infty$  to fall off as  $1/R_{\text{ex}}$ . This error is typically larger than that due to finite-difference errors, i.e., the finite extraction radius is the dominant source of error in the simulation. We estimate the mismatch error by extrapolating to  $R_{\text{ex}} \rightarrow \infty$  the mismatches between our finite-extraction-radii data. We find that the maximum mismatch (which is always at the lowest mass we consider,  $100M_\odot$ ) is  $2.8 \times 10^{-4}$ . This is much larger than the mismatch due to the numerical resolution errors, as we expect. The maximum mismatch in each case is given in Table III.

Such levels of accuracy are well within the requirements set out in [77], and also within the suggested accuracy for waveform modeling within the NR-AR project [78]. This is also comparable or better than the level of mismatch between the different equal-mass nonspinning waveforms

(taken from independent codes) that were studied in the Samurai project [13], suggesting that these waveforms are also of sufficient accuracy for GW detection purposes with current ground-based detectors. The accuracy requirements for parameter estimation, and for applications with future detectors, such as the space-based Laser Interferometric Space Antenna [79] and third-generation ground-based Einstein Telescope [80], may be much higher, but have not yet been quantified for NR waveforms.

## VI. PHYSICAL PROPERTIES OF THE BINARY CONFIGURATIONS

Now that we have established the accuracy of our simulations, we can calculate some of their physical properties. The most accurate are quantities calculated from the phase and amplitude of the leading harmonic, like the mass and spin of the final black hole. Less accurate are integrated quantities based on the leading subdominant harmonics, like the radiated energy in each mode. The gravitational recoil, which is not only based on the higher harmonics, but on overlaps between some of the weaker harmonics, is the least accurate. We will consider first the general physical properties of the binary configurations.

### A. General properties

In Table IV we indicate the initial coordinate separation of the binary  $D/M$ , and the number of GW cycles before merger,  $N_{\text{GW}}$ . The latter quantity is defined as  $\Delta\Phi/(2\pi)$ , where  $\Delta\Phi$  is the accumulated GW phase from  $t = 200M$  (i.e., after the early burst of junk radiation) until the time when the wave’s amplitude reaches its maximum value.

The configurations we simulated for this work clearly demonstrate the orbital hang-up and “anti-hang-up”

effects for spins parallel or antiparallel to the orbital angular momentum. The orbital hang-up case was first studied in [81], and for a larger range of cases in [16]; the largest spin considered was  $\chi_i = 0.92$  in [60]. One case of antiparallel spins with  $\chi_i = -0.438$  was considered in [82].

When the black holes are nonspinning, a binary with an initial coordinate separation of  $D = 12M$  produces around 19 GW cycles before merger. When the black holes have spins  $\chi_i = 0.25$ , the merger is delayed in comparison with the nonspinning case, and a binary with the same initial separation produces 21.5 GW cycles before merger. Conversely, when the spins are  $\chi_i = -0.25$ , the merger is accelerated, and the binary produces only 18.5 GW cycles before merger. These trends continue as the spins are increased, and in order to produce comparable numbers of GW cycles in each simulation, the initial coordinate separation is increased for increasing antiparallel spins  $\chi_i < 0$ , and decreased for increasing parallel spins  $\chi_i > 0$ . For the highest-spin cases,  $|\chi_i| = 0.85$ , an initial separation of  $D = 13M$  is required to produce 16 GW cycles in the antiparallel case, and an initial separation of only  $D = 10M$  produces 20 GW cycles in the parallel case.

In the unequal-mass nonspinning cases, we see that the number of cycles before merger also varies with the mass ratio  $q$ . The general effect is best understood by considering the two extreme cases,  $q = 1$  and the extreme-mass-ratio case  $q \rightarrow \infty$ . In the extreme-mass-ratio case, i.e., a point particle orbiting a Schwarzschild black hole, the slow inspiral terminates abruptly at the innermost stable circular orbit (ISCO), and the small black hole plunges into the large black hole. Prior to the ISCO, the small black hole follows a slow adiabatic inspiral, so that there are very many orbits at separations just above the ISCO, but as soon as the small black hole passes the ISCO, there are no more

TABLE IV. Summary of the configurations simulated. The table indicates the initial coordinate separation  $D/M$  of the punctures, their tangential and radial momenta ( $p_t, p_r$ ), and the eccentricity  $e$  of the resulting coordinate motion. For the  $\chi_i < 0$  cases, where enhanced PN parameters were used to achieve low-eccentricity inspiral, the eccentricity from raw PN-inspiral parameters is also shown in brackets. The initial GW frequency is  $M\omega_i$ , and the ringdown frequency of the final merged black hole is  $M\omega_{\text{RD}}$ . The simulation includes  $N_{\text{GW}}$  cycles before the peak of the GW amplitude, which occurs at  $t_{\text{peak}}$ . The final black hole has mass  $M_f$  and spin  $a_f$ , and receives a recoil of  $v_{\text{kick}}$ .

| $q$ | $S_i/M_i^2$ | $D/M$ | $p_t/M$  | $-p_r/M(\times 10^{-4})$ | $e$             | $M\omega_i$ | $N_{\text{GW}}$ | $t_{\text{peak}}/M$ | $M\omega_{\text{RD}}$ | $M_f/M$ | $a_f/M_f$ | $v_{\text{kick}}$ (km/s) |
|-----|-------------|-------|----------|--------------------------|-----------------|-------------|-----------------|---------------------|-----------------------|---------|-----------|--------------------------|
| 1   | -0.85       | 13.0  | 0.084542 | 5.247                    | 0.0025 (0.009)  | 0.040       | 16              | 1868                | 0.457                 | 0.969   | 0.412     | 0                        |
| 1   | -0.75       | 13.0  | 0.084057 | 5.060                    | 0.0016 (0.008)  | 0.0395      | 17              | 2036                | 0.466                 | 0.968   | 0.446     | 0                        |
| 1   | -0.50       | 12.5  | 0.085124 | 5.258                    | 0.0029 (0.0045) | 0.042       | 18              | 2065                | 0.490                 | 0.965   | 0.531     | 0                        |
| 1   | -0.25       | 12.0  | 0.086312 | 5.623                    | 0.0025 (0.004)  | 0.044       | 18.5            | 1955                | 0.519                 | 0.959   | 0.609     | 0                        |
| 1   | 0           | 12.0  | 0.085035 | 5.373                    | 0.0018          | 0.044       | 19              | 1939                | 0.553                 | 0.951   | 0.686     | 0                        |
| 1   | 0.25        | 12.0  | 0.083813 | 0                        | 0.0061          | 0.043       | 21.5            | 2129                | 0.595                 | 0.942   | 0.760     | 0                        |
| 1   | 0.50        | 11.0  | 0.087415 | 0                        | 0.0061          | 0.049       | 20              | 1739                | 0.650                 | 0.936   | 0.832     | 0                        |
| 1   | 0.75        | 10.0  | 0.091435 | 0                        | 0.0060          | 0.055       | 19              | 1432                | 0.728                 | 0.921   | 0.898     | 0                        |
| 1   | 0.85        | 10.0  | 0.090857 | 0                        | 0.0050          | 0.055       | 20              | 1492                | 0.770                 | 0.895   | 0.915     | 0                        |
| 2   | 0           | 10.0  | 0.085599 | 7.948                    | 0.0023          | 0.058       | 12.5            | 1069                | 0.522                 | 0.962   | 0.623     | $140 \pm 5$              |
| 3   | 0           | 10.0  | 0.072408 | 5.802                    | 0.0016          | 0.058       | 14.5            | 1240                | 0.489                 | 0.972   | 0.540     | $155 \pm 15$             |
| 4   | 0           | 10.0  | 0.061914 | 4.333                    | 0.0038          | 0.056       | 17              | 1461                | 0.467                 | 0.978   | 0.471     | $145 \pm 10$             |
| 4   | 0           | 10.0  | 0.061883 | 4.211                    | 0.0026          | 0.057       | 16              | 1396                | 0.467                 | 0.978   | 0.471     | $145 \pm 10$             |



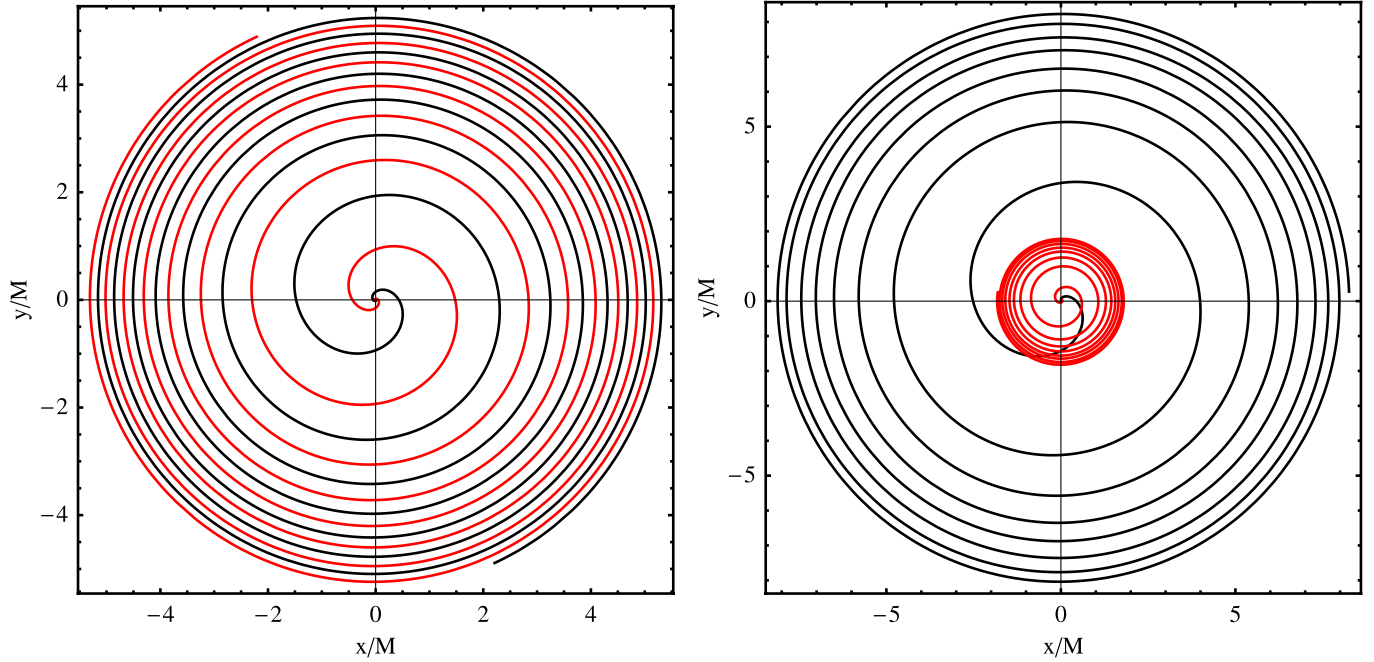


FIG. 4 (color online). Puncture motion for the nonspinning binary configurations  $q = 1$  (left) and  $q = 4$  (right). The figure shows about seven orbits before merger for each system. In the  $q = 4$  case, the black line indicates the small black hole, while the red line indicates the large black hole. Note that the transition from inspiral to plunge and merger is more gradual in the  $q = 1$  case. As the mass ratio increases, the plunge begins to resemble the ISCO effect that is present for extreme mass ratios.

orbits, only the fast plunge. By contrast, in the equal-mass nonspinning case, the transition from “inspiral” to “plunge” is very smooth, and there is no ISCO; the rate of inspiral simply increases. As the mass ratio is increased, the rate of the “plunge” increases, and the rate of inspiral prior to merger decreases—in other words, the dynamics approach the extreme-mass-ratio situation, and the system gets closer to exhibiting an ISCO. This behavior is illustrated in Fig. 4.

### B. Final mass and spin

The final mass of the merged black hole can be estimated from the energy lost through gravitational radiation. Given the total (ADM) energy in the initial data,  $E_{\text{ADM}}$ , and the radiated energy  $E_{\text{rad}}$ , we know that the final spacetime must contain the energy  $M_f = E_{\text{ADM}} - E_{\text{rad}}$ . Since the final spacetime contains only a single stationary (i.e., non-radiating) Kerr black hole,  $M_f$  must be the mass of that black hole.

We calculate the radiated energy  $E_{\text{rad}}$  on each of the five extraction spheres  $R_{\text{ex}} = \{50, 60, 70, 80, 90\}M$ , and extrapolate the result to  $R_{\text{ex}} \rightarrow \infty$  assuming that the error falls off as  $1/R_{\text{ex}}$ . This assumption is most consistent with the data at the largest extraction radii, and so we use only  $R_{\text{ex}} = \{70, 80, 90\}M$  for the fit, and include also  $R_{\text{ex}} = 60M$  to assess the robustness of the result. Once  $E_{\text{rad}}$  has been estimated for each resolution, we find that the results converge at roughly fourth order, although since the convergence is not extremely clean, we use second-, fourth-,

and sixth-order Richardson-extrapolated values to estimate the uncertainty in the value from the highest-resolution simulation. In all cases we consider the uncertainty in the radiated energy to be about 2%. The values of the mass of the final black hole are given in Table IV.

To estimate the spin of the final black hole, we make use of analytic results that give the quasinormal ringdown frequency  $M_f \omega_{\text{RD}}$  in terms of the black-hole spin,  $a_f/M_f$  [83]. In the ringdown regime, the GW signal behaves as  $\sim \exp(-i\omega_{\text{RD}}t)$ , where  $\omega_{\text{RD}}$  consists of a real part (which is the frequency of the ringdown waveform), and an imaginary part, which describes the rate of exponential falloff. Given the final mass  $M_f$  and the ringdown waveform, we can estimate the final spin using either the exponential decay-rate of the wave’s amplitude, or the wave’s frequency  $M\omega$  in the ringdown stage. We find that matching to the ringdown frequency gives the most accurate results, in the sense that both methods agree within uncertainties, but the uncertainty estimates are smaller when we match to the ringdown frequency. In general our final spin estimates have an uncertainty of 1%, although it is a little smaller in the  $\chi_i = 0.85$  case, which we now consider in more detail.

In the  $\chi_i = 0.85$  case, we find that the ringdown frequency is  $M\omega_{\text{RD}} = 0.769 \pm 0.001$ ; see Fig. 5. The final mass is  $M_f/M = 0.895 \pm 0.015$ , and the final spin is  $a_f/M_f = 0.915 \pm 0.007$ . Note that the final mass is lower than quoted in [16], where all of the analysis was performed on the highest-resolution waveform calculated on

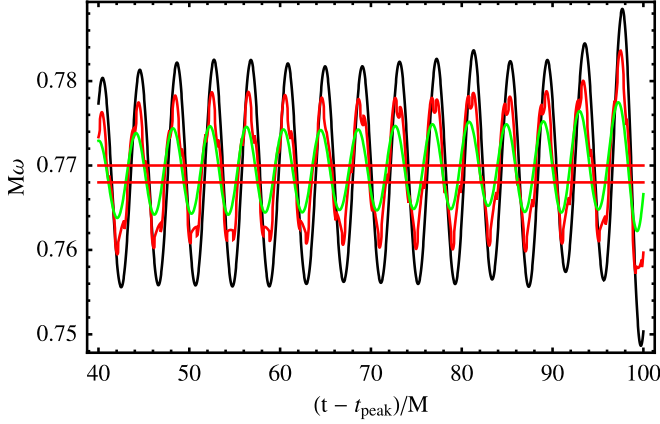


FIG. 5 (color online). The numerical GW frequency at a time  $(t - t_{\text{peak}})/M$  after the peak of  $|r\Psi_{4,22}|$ , shown for simulations at three resolutions. The frequency oscillates around a value that we take to be the ringdown frequency. The amplitude of the oscillations decreases as the numerical resolution is improved, suggesting that these are only a numerical artifact. The upper and lower bounds of our estimate of the ringdown frequency are indicated by the two horizontal lines in the plot. The bounds were obtained by considering the results from all three numerical resolutions, and varying the portion of the data used for the fit; the final quoted values were calculated using the range  $(t - t_{\text{peak}})/M \in \{50, 100\}$ . Despite the high amplitude of the noise in the data, the average value shows very little variation, and can be estimated with an uncertainty of only  $\Delta\omega = 0.001/M$ .

the largest radiation extraction sphere. Here we extrapolate the results with respect to extraction radius (assuming a  $1/R_{\text{ex}}$  falloff in the error), and with respect to numerical resolution, where the results show between second- and sixth-order convergence. The radiated energy increases with extraction radius, and so our estimate of the final mass decreases; this is why our extrapolated value (0.895) is lower than the  $R_{\text{ex}} = 90M$  value of 0.911 quoted in [16]. In addition, we estimate the ringdown frequency using a  $50M$ -long sample of the waveform starting  $50M$  after the peak amplitude of the  $(\ell = 2, m = 2)$  mode, while our earlier results were based on a portion of the waveform starting only a few  $M$  after the peak amplitude, which distorts the final estimate of the ringdown frequency.

For comparison, Dain *et al.* [60] study the  $\chi_i = 0.92$  case. The initial black-hole spins are larger than studied here (and were set up to approach the highest spin possible for Bowen-York data), and therefore the final black holes should have a larger ringdown frequency than in our  $\chi_i = 0.85$  case, and a higher final spin, and this is indeed the case. Note that they use the ADM mass  $M_{\text{ADM}}$  as the defining length scale in their simulations, while we use the total black-hole mass. In terms of the ADM mass, the ringdown frequency for the  $\chi_i = 0.85$  case is  $M_{\text{ADM}}\omega_{\text{RD}} = 0.761$ , while the frequency found in [60] for the  $\chi_i = 0.92$  case is  $M_{\text{ADM}}\omega_{\text{RD}} = 0.766$ . In addition, they give a measure of the final spin between 0.910 and 0.916,

where 0.915 is the value obtained using the same quasinormal-mode method that we have applied here. Their final spin result is consistent with ours' within our error bounds.

A number of aligned-spin cases were studied in [84]. For the cases where direct comparison is available, our results show agreement within 1% for spins up to 0.5, and within 2% for higher spins. Assuming that their uncertainties are comparable to ours, then the results agree. The first hang-up and anti-hang-up cases were studied in [81], each with spin values of  $|\chi_i| = 0.757$ . They estimate final spins of 0.443 and 0.890 for the anti-hang-up and hang-up cases, respectively, and these are also consistent with our results. Two of the unequal-mass cases were also studied in [70],  $q = 2, 4$ , and the final mass and spin results are in excellent agreement.

We have also compared our results with fits for the final spin available in the literature. We find excellent agreement to about 1% or better with [85], as well as with [86] as long as the spins are not anti-aligned with the orbital angular momentum. For the latter paper we find disagreements of  $\approx 10\%$  for the cases  $\chi_i = -0.75, -0.85$ .

### C. Energy spectrum in spherical harmonic modes

The  $(\ell = 2, m = 2)$  mode dominates the GW signal from a black-hole-binary coalescence, and indeed most current searches in detector data employ templates that include only this harmonic [87,88] (see also the NINJA project searches in simulated data with injected numerical relativity waveforms [10,11]). However, knowledge of the subdominant modes may aid detection, and are important for accurate estimation of the source parameters [64,89–92].

We assess the relative importance of the subdominant modes by calculating the energy radiated in each mode. The radiated energy in each mode is given by [93]

$$\frac{dE_{\ell,m}}{dt} = \lim_{r \rightarrow \infty} \frac{r^2}{16\pi} \left| \int_{-\infty}^t \Psi_{4,\ell m} dt' \right|^2. \quad (6)$$

In practice the limits of the integration are taken as the time in the simulation just after the junk radiation has passed, and a time after the signal has rung down to the level of numerical noise. The results are summarized in Table V, including only those modes that contribute above 1% of the total energy. We see that in the equal-mass cases, the  $(2, 2)$  mode dominates—around 98% of the energy is radiated in the dominant mode in all cases, with only a negligible variation due to spin, and no other modes contribute above 1%.

In the unequal-mass cases, the energy contribution from the higher harmonics grows rapidly with mass ratio, particularly in the  $\ell = \pm m$  modes. We defer the reader to the detailed discussion in [94], but note that, even at  $q = 4$ , most of the energy is radiated in a very small number of harmonics.

TABLE V. Ratio of total energy radiated in each mode. Only contributions above 1% are included.

| Case             | (2, $\pm 2$ ) | (2, $\pm 1$ ) | (3, $\pm 3$ ) | (4, $\pm 4$ ) | (5, $\pm 5$ ) |
|------------------|---------------|---------------|---------------|---------------|---------------|
| $\chi_i = -0.85$ | 0.988         | 0             | 0             | ...           | 0             |
| $\chi_i = -0.50$ | 0.989         | 0             | 0             | ...           | 0             |
| $\chi_i = 0$     | 0.990         | 0             | 0             | ...           | 0             |
| $\chi_i = 0.50$  | 0.988         | 0             | 0             | ...           | 0             |
| $\chi_i = 0.85$  | 0.988         | 0             | 0             | ...           | 0             |
| $q = 2$          | 0.947         | ...           | 0.038         | ...           | ...           |
| $q = 3$          | 0.897         | ...           | 0.076         | 0.013         | ...           |
| $q = 4$          | 0.868         | 0.013         | 0.095         | 0.017         | ...           |

### D. Recoil

Because of the asymmetry of the radiation emission in the unequal-mass cases, linear momentum is radiated from the system, and the center of mass of the binary moves as the black holes inspiral. The direction of the center of mass recoil rotates with the binary, so that the average movement is small. However, the rate of momentum loss grows as the black holes get closer, and, as with the total GW signal, peaks at merger. This final burst of GW emission causes an overall recoil, or “kick.”

Since the bulk of the recoil arises during the merger, short simulations are sufficient to accurately measure the effect, and these were used in [25,95,96] to make the first accurate fully general-relativistic predictions of gravitational recoil, and found that the maximum kick for nonspinning binaries is  $v_{\text{max}} = 175 \pm 11$  km/s for a mass ratio of  $q = 2.8$  [25]. An analytical fitting formula for the recoil from nonspinning binaries was presented in [25], for recent papers containing such fitting formulas see [97] (which uses the same ansatz as [25] and finds slightly different but consistent fitting parameters) and [86] (which quotes the fit from [25] for nonspinning binaries).

Table IV shows the results for the current simulations, which agree with those from the shorter simulations presented in [25]. It has also been shown that much larger recoils are possible from spinning or highly elliptical binaries [26,60,98–105], but not for any of the configurations that we have studied in this work.

Our newer simulations improve over those produced in [25] in two ways: they include many more cycles before merger, and the wave extraction is performed at larger radii. On the other hand, the numerical resolution at the wave extraction radii is lower, which reduces the accuracy. As such, the values we quote in Table IV have large error bars.

The flux of angular momentum radiation is given by

$$\frac{dP_i}{dt} = \lim_{r \rightarrow \infty} \left[ \frac{r^2}{16\pi} \int_{\Omega} \ell_i \left| \int_{-\infty}^t \Psi_4 d\tilde{t} \right|^2 d\Omega \right], \quad (7)$$

where  $\ell_i = (\sin\theta \cos\phi, \sin\theta \sin\phi, \cos\theta)$  [106]. The total recoil is calculated by integrating Eq. (7) over the duration of the simulation.

The additional length of the new simulations allows us to remove one source of error in shorter simulations: the choice of starting time in the integration of  $dP_i/dt$  to calculate the total radiated linear momentum. This function oscillates with time, and during the inspiral the average radiated linear momentum is much smaller than the amplitude of the oscillations—so a poor choice of starting time in the integration of  $dP_i/dt$  could potentially corrupt the final result. In [25] the uncertainty due to this effect was estimated at about 3%. In [95,98] attempts were made to both account for this effect and for the linear momentum loss that will have accumulated over the earlier inspiral of the binary. In our cases, where we possess the waveform for many more cycles before merger, we are able to simply calculate the total recoil for a range of integration starting times  $t_0$ , and then to take the average of these values. We find that the uncertainty in this process is only a fraction of a percent of the final result.

Figure 6 illustrates this effect with the  $q = 4$  case. The lower limit of the integration,  $t_0$ , was varied between  $t_0 = 125M$  (just after the burst of junk radiation has passed through the signal, and  $t_0 = 1200M$ , which is about  $300M$  before  $dP_i/dt$  has fallen to negligible values, and also roughly corresponds to the value of  $t_0$  that was used for the much shorter waveforms studied in [25]. Note that the kick calculated for different choices of  $t_0$  varies by about 4 km/s, or 3% of the result. A linear curve fit through the results (shown in the figure) indicates that the average result of the integrated linear momentum radiation rises very slowly during the inspiral, and varies by only 0.7 km/s, or 0.5%. In our results, we determine the final kick to be the average over this range of choices  $t_0$ , which introduces only a negligible error in our result.

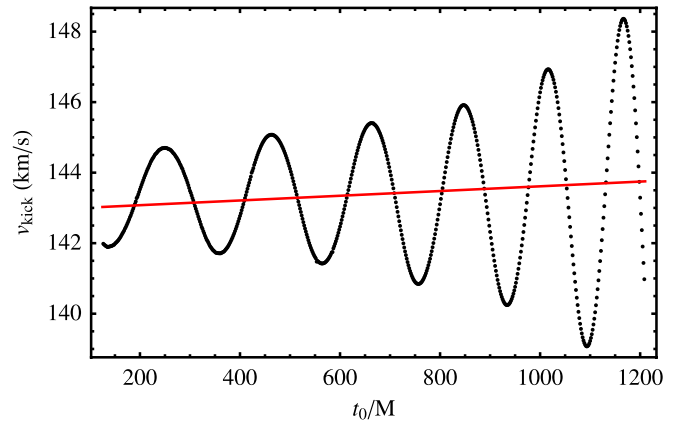


FIG. 6 (color online). Variation in the estimate of the total radiated linear momentum (recoil), as a function of the starting time  $t_0$  of the integration of  $dP_i/dt$  for the  $q = 4$  case. The value oscillates around a slowly growing average, which is indicated by a straight line. Note that the latest integration time used,  $t_0 = 1200M$ , is approximately  $300M$  before the end of the ringdown, which is the point at which the integration was started in the older calculations in [25].

A second error source that could not be quantified in [25] was that due to extraction of the GW signal at finite extraction radius. In that work an extraction radius of only  $R_{\text{ex}} = 30M$  was feasible. We now extract GW signals at up to  $R_{\text{ex}} = 90M$ , although we find that the numerical resolution at the wave extraction spheres allows an accurate calculation of the recoil only for  $R_{\text{ex}} = \{50, 60\}M$ . However, these two radii are sufficient for us to extrapolate the recoil to  $R_{\text{ex}} \rightarrow \infty$ , assuming a  $1/R_{\text{ex}}$  falloff in the error. This gives the values listed in Table IV. This fit also of course predicts the value of the recoil at  $R_{\text{ex}} = 30M$ , which agrees well with the values in [25]. However, due to the poorer numerical resolution on the extraction spheres, we assign large error bars to our values.

## VII. LATE INSPIRAL COMPARISON OF NR AND PN WAVEFORMS

One of the most important applications of our waveforms is as input in the construction of analytic waveform models that can in turn be used to construct template banks for GW searches. In particular, these waveforms have already been used to produce the phenomenological models presented in [36,56,65,67], in which the NR waveforms for the late inspiral and merger are connected to long PN inspiral waveforms, to produce “complete” waveforms for the full inspiral-merger-ringdown, and it is these complete waveforms that are then used in the construction of a phenomenological model that is essentially an analytic fit across the relevant section of the black-hole-binary parameter space.

In performing this procedure, we need to quantify the level of agreement between the PN and NR waveforms in some region where they are both considered to be valid. In other words: the approximate PN waveforms are expected to be accurate during much of the long inspiral, but are they still accurate enough at the point where we want to connect them to fully general relativistic results?

This question was first addressed for equal-mass non-spinning waveforms in [69,107], and later with increasing levels of precision in [14,15,68]. The conclusion of these works was that the phase disagreement between NR waveforms and typical PN approximants was less than 1 rad over the last 10 cycles up to  $M\omega = 0.1$ , and the error in the quadrupole PN amplitude was about 8%; however, the phase could be tracked with surprising accuracy by one PN approximant, TaylorT4, and the PN amplitude was accurate to within 2% when evaluated at 3PN order [68,108].

Similar comparisons were performed with the equal-mass  $\chi_i > 0$  cases that we consider here, where it was found that the phase disagreements were comparable for all spin values for the TaylorT1 approximant (i.e., approximately 1 rad over the 10 cycles up to  $M\omega = 0.1$ ), but that the TaylorT4 approximant, which performed so well in the nonspinning case, did no better than TaylorT1 (and often worse) when the

black holes were spinning. It should be noted, however, that the Taylor approximants did not include spin terms up to the same PN order as in nonspinning terms (2.5PN versus 3.5PN), which is a point we will return to later. In addition, it was found that the quadrupole amplitude error grew to as much as 12% in high spin cases [16]. Equal-mass non-spinning eccentric binaries were considered in [109], and one unequal-mass precessing-spin configuration was studied in [37].

In this section we will perform a PN-NR comparison for all of our waveforms, which now include  $q \neq 1$  and  $\chi_i < 0$  cases.

### A. PN approximants

The PN approximants considered here are derived from the energy  $\mathcal{E}$  and GW flux  $\mathcal{F}$  of a black-hole binary on quasicircular orbits. Both quantities are given in the PN framework as expansions in  $v/c$ , up to  $(v/c)^7$  (3.5PN order), where  $v$  is the relative velocity and  $c$  the speed of light. Following the standard convention, we regard  $\mathcal{E}$  and  $\mathcal{F}$  as functions of the dimensionless variable  $x = (v/c)^2$  that is related to the orbital phase  $\phi_{\text{orb}}$  via

$$x = (M\omega_{\text{orb}})^{2/3}, \quad \frac{d\phi_{\text{orb}}}{dt} = \omega_{\text{orb}}. \quad (8)$$

The energy-balance law  $d\mathcal{E}/dt = -\mathcal{F}$  can be transformed to an evolution equation for  $x$ ,

$$\frac{dx}{dt} = -\frac{\mathcal{F}}{d\mathcal{E}/dx}, \quad (9)$$

which in turn leads to the  $\ell m$  mode of the gravitational wave strain

$$h^{\ell m}(t) = H^{\ell m}(t)e^{-im\phi_{\text{orb}}(t)}. \quad (10)$$

The amplitudes  $H^{\ell m}$  are given as expansions in  $x$  to 3PN order in the nonspinning case [110] and up to 2PN order in spinning contributions [59].

A direct (numerical) integration of (9) and (8) is referred to as the *TaylorT1* approximant. If instead the right-hand side of Eq. (9) is re-expanded as a Taylor series in  $x$  before integrating, the resulting approximant is called *TaylorT4*. This re-expansion is truncated at the same order as the energy and flux (i.e., 3.5PN); all higher powers in  $x$  are incomplete and therefore neglected.

If we apply the same strategy to the spin contributions that enter at 1.5PN (leading-order spin-orbit coupling), 2PN (spin-spin) and 2.5PN order (next-to-leading-order spin orbit), we should neglect all spin-dependent terms in the re-expansion of (9) that appear at 3PN and 3.5PN order. We denote the resulting approximant that was used for instance in [16] as *TaylorT4 (truncated)*. If we instead disregard the distinction of spinning and nonspinning terms and use the “full” re-expansion up to 3.5 PN order, thereby keeping incomplete spin contributions at 3 and 3.5PN order, we denote the resulting approximant simply



as *TaylorT4*. For a detailed discussion and explicit expressions for the approximants see [67] and references therein. Further small corrections to the spin contributions to the PN phase and amplitude, due to typographical or other errors in the original literature, were found during a program of PN-approximant verification within the Ninja collaboration [78]; these will be described in more detail in an upcoming amendment to the data format specification document [111], and are discussed further in Sec. VII C below.

### B. Phase comparison

We now compare the PN and NR phase. Our procedure, as in previous studies [14,16], is to consider the phase for the  $N$  GW cycles up to the matching frequency  $M\omega_m = 0.1$ . We line up the PN and NR phase functions so that they agree when  $\omega = \omega_m$ , and relabel this event as  $t = 0$ . We then calculate the phase disagreement as it accumulates over  $N$  cycles back in time. Note that although our comparison is over a fixed number of GW cycles, it is *not* over a fixed frequency range, due to the different frequency evolution in each configuration. In the same way, the comparison is also over different lengths of time between different configurations. However, we have found that the qualitative behavior of the comparison results does not depend on whether we compare over a fixed range of cycles, frequency, or time.

In previous studies we simply calculated the phase difference  $\Delta\phi(t) = \phi_{\text{PN}}(t) - \phi_{\text{NR}}(t)$ , and quoted  $\Delta\phi(t_N)$  as the accumulated phase difference, where  $t_N$  is the time  $N$  cycles prior to the point where  $\omega = \omega_m$ . This procedure gives consistent results, but we may worry in general that  $\Delta\phi(t)$  is not a monotonic function, and so a more robust procedure is to consider instead

$$\overline{\Delta\phi}(t_N) = \frac{1}{\sqrt{-t_N}} \left[ \int_{t_N}^0 (\phi_{\text{NR}}(t) - \phi_{\text{PN}}(t))^2 dt \right]^{1/2}. \quad (11)$$

This gives us a measure of the average rate of increase of the phase disagreement. A similar procedure was also used in [112], although in that study the alignment of the waveforms was adjusted to minimize  $\overline{\Delta\phi}$ . An elegant alternative measure of the accumulated phase disagreement is given in Eq. (3.15) of [113]. We instead wish to evaluate how well the PN phase evolution agrees with the fully general relativistic NR results. For comparison with previous results in the literature, we will also show the results of a direct calculation of  $\phi_{\text{PN}}(t) - \phi_{\text{NR}}(t)$ .

Figure 7 shows the disagreement between the PN and NR phase for the equal-mass configurations with nonprecessing spins over  $N = 10$  GW cycles. Three PN approximants are used: TaylorT1, TaylorT4, and TaylorT4-truncated, as described in the previous section.

We see that in both calculations of the accumulated phase disagreement, TaylorT1 is the most robust. It performs best in the nonspinning case (which is to be

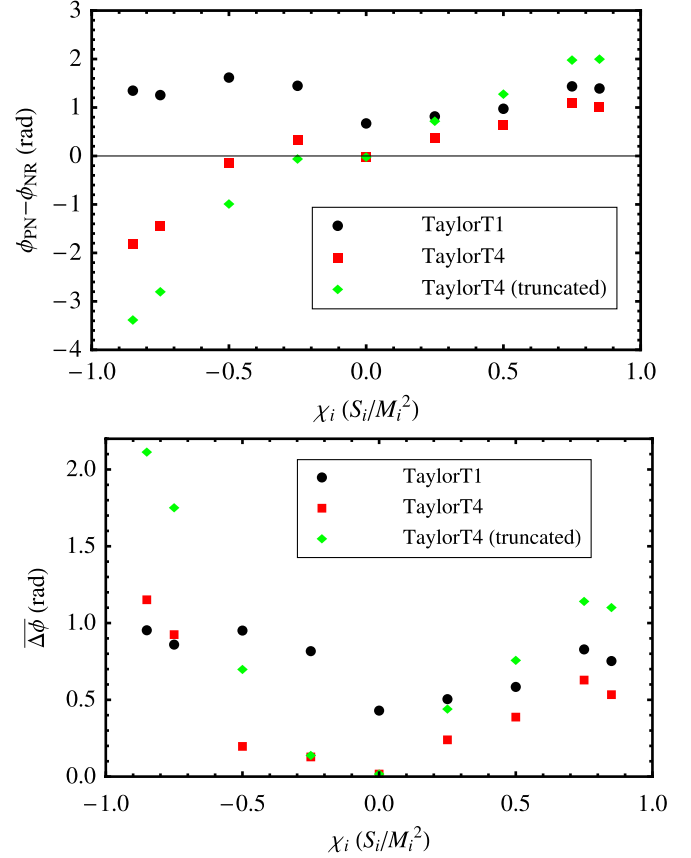


FIG. 7 (color online). Phase disagreement between NR and PN results for three choices of PN approximant, for configurations that consist of equal-mass binaries with equal spins oriented parallel or antiparallel to the orbital angular momentum. The first panel shows the accumulated phase disagreement for the ten GW cycles up to  $M\omega_m = 0.1$ . The second panel shows the integrated square of the phase disagreement, Eq. (11).

expected, since the nonspinning contributions are known to higher PN order than the spinning contributions), and for all spinning cases the accumulated phase disagreement is between 1.0 and 2.0 rad, while the square-averaged phase disagreement is between 0.5 and 1.0 rad. We see also that TaylorT4-truncated performs worse as the spin is increased, and for large anti-aligned spins performs very poorly. The full TaylorT4 approximant performs better for most spin values, although it is again poor for large anti-aligned spins. It is in light of comparisons using only TaylorT1 and TaylorT4-truncated that we chose to use the TaylorT1 approximant in the construction of hybrid waveforms for the phenomenological model in [56].

Figure 8 shows a similar plot, but this time for the unequal-mass nonspinning configurations. The  $q = 2$  simulations consist of less than ten cycles before  $M\omega = 0.1$ , so we consider only  $N = 8$  cycles in the phase comparison. In this case we see that TaylorT4 continues to perform well for unequal-mass configurations. We expect that at higher mass ratios the performance of all PN approximants will deteriorate, but up to  $q = 4$  this

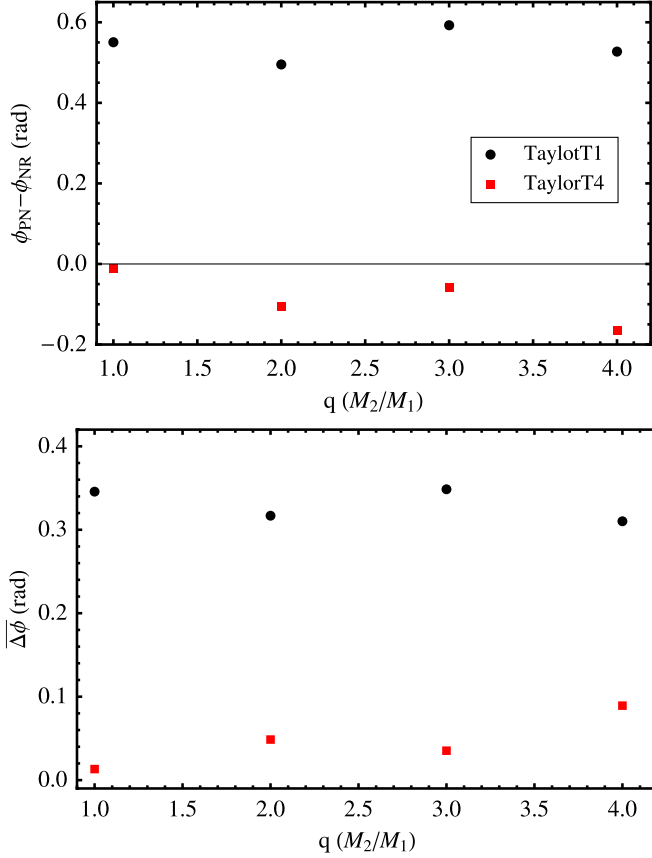


FIG. 8 (color online). Phase disagreement between NR and PN results for two choices of PN approximant, for configurations that consist of nonspinning black holes of unequal mass, with mass ratio  $q = M_2/M_1$ .

deterioration cannot be clearly measured; the performance of TaylorT1 and TaylorT4 shows some variation with mass ratio, but this is not monotonic.

From our phase comparison analysis, we conclude that the TaylorT1 approximant is most robust over the entire subset of the black-hole-binary parameter space that we have studied. The TaylorT4 approximant performs well for all nonspinning cases. The performance of TaylorT4 for spinning cases varies greatly between our two choices of treatment of the higher-order spin contributions, but for both choices shows poor agreement for large anti-aligned spins. We caution, however, that the performance of the approximants over a relatively small number of numerical cycles does not tell us how well they perform before at lower frequencies, and we will return to this point in the Discussion.

### C. Amplitude comparison

We now compare the PN prediction for the inspiral wave amplitude with numerical results, for the ( $\ell = 2, m = 2$ ) mode. We found in [14] that in the equal-mass nonspinning case the quadrupole PN amplitude was larger than the full GR amplitude during inspiral by about 7%. It was later

shown in [68] that the amplitude agreement could be improved to within 2% if corrections up to 3PN order were used. For equal-mass binaries with aligned spins, we found in [16] that the quadrupole PN amplitude disagreement rose to about 12% in highly spinning cases.

In this section we extend our previous analysis of the quadrupole amplitude to anti-aligned and unequal-mass cases. We also compare with the PN amplitude that results from using all currently known amplitude corrections (up to 3PN order nonspinning [108,110] and up to 2PN order spinning contributions [59,114]). We have taken care when combining results for amplitude functions from different sources in the literature, in particular, regarding different conventions for the choice of relative phase factors. In our implementation we now follow the convention of [59], which differs from that of [110], from which we originally took our nonspinning amplitude contributions. We have checked for consistency with the amplitude of the  $l = |m| = 2$  modes as given in [115], and we have compared with an independent code as part of the Ninja project [78,116]. In addition, we have also checked that inconsistent choices of the relative phase factors (e.g., caused by misprints in the literature) significantly increase the deviation of the NR and PN amplitudes; the correct choices lead to the best agreement with results from full general relativity.

We find that the GW amplitude shows variations with numerical extraction radius that are comparable to the level of disagreement with the PN predictions. However, the error in the amplitude seems to fall off as  $1/R_{\text{ex}}^2$  (see [14] for a discussion of this effect), and allows us to perform an accurate extrapolation to  $R_{\text{ex}} \rightarrow \infty$ . Having obtained the accurate amplitude of  $R_{\text{ex}}\Psi_4$ , we then express the amplitude as a function of frequency, using the methods we introduced in Sec. VB, which then allows us to easily compare with the PN amplitude, which is always expressed as a function of frequency. Note that for this comparison we perform a frequency fit to our data during only the inspiral, which allows us to much more accurately capture the amplitude evolution; it is now much more necessary than in Sec. VB to have a reliable *physical* fit.

Figure 9 shows the average disagreement between the PN and NR amplitudes over the 10 cycles up to  $M\omega = 0.1$ , for the equal-mass spinning cases. The results using both the quadrupole and 3PN order amplitudes are shown. As seen in [16] the quadrupole amplitude disagreement rises to just over 12% for the highly spinning cases. The increase in disagreement is approximately linear with respect to the spin, and we predict that the maximum disagreement for extreme-spin black holes would be around 14%. For large antiparallel spins, the quadrupole amplitude performs much better, and drops to around 3% for  $\chi_i = -0.85$ .

When PN amplitude contributions up to 3PN (nonspinning)/2PN (spinning) order are used, the agreement with NR results is much better. In the nonspinning case it is 3%,

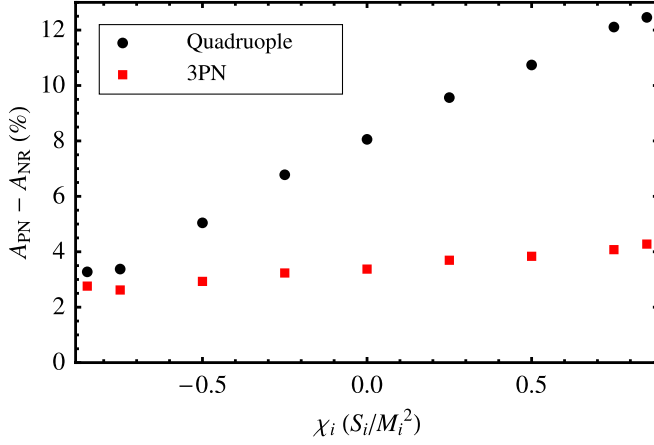


FIG. 9 (color online). Average amplitude disagreement between PN and NR results, over the last ten cycles up to  $M\omega = 0.1$ . The quadrupole PN amplitude error is only about 3% for large anti-aligned spins, but rises to around 13% for large aligned spins. When the amplitude corrections are included up to 3PN order, the PN amplitude error is only 3–4% for all spin values.

consistent with the results in [68]. (Note that the uncertainty in the extrapolated NR amplitude is around 1%.) The variation with spin is small, rising to only 4% in the high-spin hang-up cases, and falling to 2.5% in the high-spin anti-hang-up cases. We find similar results for the unequal-mass cases, where the average disagreement is around 3%.

### VIII. DISCUSSION

We have presented the results of two sets of numerical simulations of black-hole binaries, equal-mass binaries with equal, nonprecessing spins with  $\chi_i = S_i/M_i^2 \in [-0.85, 0.85]$ , and nonspinning unequal-mass binaries with  $q = M_2/M_1 \in [1, 4]$ . These simulations cover between six and 10 orbits before merger. The most accurate simulations have a numerical phase uncertainty during inspiral of 0.05 rad, and a total accumulated phase error of about 1.0 rad. The phase uncertainties in the least accurate case are 0.1 rad during inspiral, and a total accumulated phase error of up to 15 rad. We have shown, however, that the uncertainty estimates depend strongly on the alignment of the waveforms, and whether the results are represented as functions of time or of GW frequency. The accuracy of the amplitude of the  $(\ell = 2, m = 2)$  mode of  $\Psi_4$  is in general better than 1% during inspiral, and between 2% and 5% during merger.

For purposes of GW detection, the important quantity to consider is the mismatch error in the waveform. This is dominated by the errors due to the extraction of the GW signal at a finite radius from the source. However, in all cases the mismatch error (minimized over only time and phase) is below  $10^{-5}$ , meaning that the numerical waveforms are well within the accuracy requirements for detection with current and planned ground-based detectors.

These statements of waveform accuracy for detection apply only to the dominant mode and, more importantly, are only relevant when we consider binary masses such that the entire numerical waveform is within the sensitivity band of the detector,  $M \gtrsim 120M_\odot$ . For lower masses, longer waveforms are required, and in general can be produced by connecting PN and NR waveforms [36,65,67,117,118]. The accuracy estimates given in this paper tell us *nothing* about the accuracy of such longer “hybrid” waveforms, because we cannot properly quantify the accuracy of the PN approximants. We defer the discussion of the accuracy of hybrid waveforms, and the implications for the necessary length of numerical waveforms, to separate work [119].

For now we consider the fidelity of PN results to full general relativity only in the regime where we also have NR results, i.e., in the last orbits before merger. We compare the PN and NR phase disagreement over the last 8–10 GW cycles before  $M\omega = 0.1$  for two classes of PN approximant, TaylorT1 and TaylorT4. For nonspinning cases we find that the performance of both approximants does not change drastically as the mass ratio is increased to  $q = 4$ , and this means that the TaylorT4 approximant continues to provide the best agreement, with an accumulated phase disagreement in the  $q = 4$  case of 0.2 rad, or 0.1 rad if we consider the root-mean-square average of the phase disagreement; see Fig. 8. For spinning binaries, the two approximants include spin terms up to only 2.5PN order. The TaylorT1 approximant nonetheless is fairly robust, while TaylorT4-truncated performs poorly for large spins, in particular, large spins anti-aligned with the binary’s orbital angular momentum. The full TaylorT4 approximant performs well for all spins larger than  $\chi_i = -0.75$ .

Finally, we study the accuracy of the PN wave amplitude, and find that when the highest-order amplitude corrections are included (3PN for nonspinning binaries, and 2PN for spinning cases), the amplitude error is no more than 4%. This is in contrast to the quadrupole amplitude, which can overestimate the true physical amplitude by up to 13% at black hole dimensionless spins of  $\chi_i = +0.85$  corresponding to an increase of 44% in detection rates. Note that precisely the cases with the largest signal-to-noise ratio (spins aligned with the angular momentum) are also those with the largest PN amplitude errors.

### ACKNOWLEDGMENTS

We thank M. Boyle for extensive cross-checks of the spin-dependent terms in the phase and amplitude of the PN approximants used in this paper. M. Hannam was supported by FWF Lise-Meitner Grant No. M1178-N16 and Science and Technology Facilities Council Grant No. ST/H008438/1, and thanks the Department of Physics at the University of the Balearic Islands for hospitality while some of this work was carried out. S. Husa was supported by Grant No. FPA-2007-60220 from the

Spanish Ministry of Science, the Spanish MICINN's Consolider-Ingenio 2010 Programme under MultiDark Grant No. CSD2009-00064, and DAAD Grant No. D/07/13385. This work was supported in part by DFG Grant SFB/Transregio 7 “Gravitational Wave Astronomy” and the DLR (Deutsches Zentrum für Luft- und Raumfahrt). D. Müller was additionally supported by the DFG Research Training Group 1523 “Quantum and Gravitational Fields.” BAM simulations were carried out at LRZ Munich, ICHEC Dublin, on the VIENNA SCIENTIFIC CLUSTER (VSC), at MareNostrum at the Barcelona Supercomputing Center—Centro Nacional de Supercomputación (Spanish National Supercomputing Center), and CESGA, Santiago de Compostela.

### APPENDIX: APPARENT-HORIZON AND PUNCTURE ESTIMATES OF THE BLACK-HOLE MASSES

There are two methods that are commonly used to estimate the masses of black holes in puncture data, in addition to analyzing apparent horizons. The first, which is generally applicable to all black-hole data, is to make use of the area of the apparent horizon,  $A$ . The black hole's “irreducible mass”  $M_{\text{irr}}$  is given by  $M_{\text{irr}} = \sqrt{A/16\pi}$ , and the total mass can be estimated by [120]

$$M^2 = M_{\text{irr}}^2 + \frac{S^2}{4M_{\text{irr}}^2}. \quad (\text{A1})$$

A second method is to make use of the asymptotic properties of the wormhole puncture data. Each puncture represents an extra asymptotically flat end of the slice, and the ADM mass calculated at each “extra” end can be considered as a measure of the mass of that black hole. In the puncture-data construction, the momentum constraint is solved analytically by the Bowen-York conformal extrinsic curvature, and the Hamiltonian constraint is solved numerically to give the function  $u$  in the ansatz [19],

$$\psi = 1 + \frac{m_1}{2r_1} + \frac{m_2}{2r_2} + u, \quad (\text{A2})$$

where  $m_i$  parametrizes the mass of the  $i$ th black hole, and  $r_i$  is the coordinate distance to the  $i$ th black hole. The resulting data represent two black holes on a three-sheeted topology. One sheet contains two black holes, and represents the physical space that we want to describe. Each black hole has an extra sheet associated with it, which extends to an extra asymptotically flat end, and in the puncture construction those ends are compactified to points, or “punctures.”

To calculate this mass, we require only the value of the function  $u$  at the puncture. The mass is then given by

$$M_i = m_i \left( 1 + u_i + \frac{m_j}{2D} \right), \quad (\text{A3})$$

TABLE VI. The uncertainty in the apparent-horizon mass is about 0.01%, and so the horizon and puncture masses agree within uncertainty for the  $S_i/M_i^2 = \{0, 0.25\}$  cases. For higher masses, however, the discrepancy between the horizon and puncture masses is clear.

| $S_i/M_i^2$ | $M_{\text{AH}}$ | $M_{\text{puncture}}$ | Error (%) |
|-------------|-----------------|-----------------------|-----------|
| 0           | 0.500 01        | 0.500 00              | 0.002     |
| 0.25        | 0.499 98        | 0.500 00              | 0.004     |
| 0.5         | 0.499 77        | 0.500 00              | 0.046     |
| 0.75        | 0.498 15        | 0.500 00              | 0.370     |
| 0.85        | 0.495 77        | 0.500 00              | 0.846     |

where  $D$  is the coordinate distance between the two punctures. A derivation of this expression is given in [19]. The two measures of the mass that we have discussed are shown to agree within numerical uncertainty in the case of nonspinning black holes in [121]. Since the ADM mass at the puncture can be easily calculated directly from the initial data with high precision, it has become a standard tool in assessing the mass of black holes in puncture data.

However, as discussed in [62], this is only a reasonable measure of the black-hole mass for nonspinning black holes. A heuristic explanation for this effect is that the falloff of the extrinsic curvature for a boosted Bowen-York black hole is far faster towards the extra asymptotically flat ends as it is towards the “physical” end, and so the extra sheets of the topology contain far less junk radiation than the physical sheet, and the ADM mass of each of those sheets is not contaminated by very much junk radiation. In the spinning case, however, the falloff on the second sheet is the same as on the physical sheet, and so the extra sheets each contain roughly the same junk radiation as the physical space, and only for low spins will the ADM mass at the puncture be a good measure of the black-hole mass.

As an illustration of this effect, the values of the black-hole mass as given by the two methods are shown in Table VI.

For the simulations presented in this paper, the results were first produced using the puncture-mass estimates. They were then rescaled according to the results in Table VI. A rescaling of mass will have an overall effect on the time-scale of the simulations, but we found that even in the highest spin case the effect was negligible. This is most important in the comparison with PN approximants in Sec. VII, where the PN and NR results are compared assuming the same mass scale. But we find that the phase disagreement between the NR and PN results is much larger than the error due to using the incorrect black-hole mass, and does not noticeably alter the results in, for example, Fig. 7.



- [1] J. Abadie *et al.* (LIGO Scientific Collaboration), *Classical Quantum Gravity* **27**, 173001 (2010).
- [2] <http://www.ligo.caltech.edu/advLIGO>.
- [3] <https://pub3.ego-gw.it/codifier/includes/showTmpFile.php?doc=2219C=VIR-027A-09.pdf>.
- [4] R. Flaminio *et al.* (VIRGO Collaboration), Advanced Virgo White Paper, Technical Report No. VIR-NOTDIR-1390-304, 2005 (unpublished).
- [5] F. Pretorius, *Phys. Rev. Lett.* **95**, 121101 (2005).
- [6] M. Campanelli, C. O. Lousto, P. Marronetti, and Y. Zlochower, *Phys. Rev. Lett.* **96**, 111101 (2006).
- [7] J. G. Baker, J. Centrella, D.-I. Choi, M. Koppitz, and J. van Meter, *Phys. Rev. Lett.* **96**, 111102 (2006).
- [8] M. Hannam, *Classical Quantum Gravity* **26**, 114001 (2009).
- [9] I. Hinder, *Classical Quantum Gravity* **27**, 114004 (2010).
- [10] B. Aylott *et al.*, *Classical Quantum Gravity* **26**, 114008 (2009).
- [11] B. Aylott *et al.*, *Classical Quantum Gravity* **26**, 165008 (2009).
- [12] S. Husa, M. Hannam, J. A. González, U. Sperhake, and B. Brügmann, *Phys. Rev. D* **77**, 044037 (2008).
- [13] M. Hannam *et al.*, *Phys. Rev. D* **79**, 084025 (2009).
- [14] M. Hannam, S. Husa, U. Sperhake, B. Brügmann, and J. A. González, *Phys. Rev. D* **77**, 044020 (2008).
- [15] A. Gopakumar, M. Hannam, S. Husa, and B. Brügmann, *Phys. Rev. D* **78**, 064026 (2008).
- [16] M. Hannam, S. Husa, B. Brügmann, and A. Gopakumar, *Phys. Rev. D* **78**, 104007 (2008).
- [17] B. Brügmann *et al.*, *Phys. Rev. D* **77**, 024027 (2008).
- [18] S. Husa, J. A. González, M. Hannam, B. Brügmann, and U. Sperhake, *Classical Quantum Gravity* **25**, 105006 (2008).
- [19] S. Brandt and B. Brügmann, *Phys. Rev. Lett.* **78**, 3606 (1997).
- [20] J. M. Bowen and J. W. York, Jr., *Phys. Rev. D* **21**, 2047 (1980).
- [21] M. Ansorg, B. Brügmann, and W. Tichy, *Phys. Rev. D* **70**, 064011 (2004).
- [22] M. Shibata and T. Nakamura, *Phys. Rev. D* **52**, 5428 (1995).
- [23] T. W. Baumgarte and S. L. Shapiro, *Phys. Rev. D* **59**, 024007 (1998).
- [24] A. H. Mroue, H. P. Pfeiffer, L. E. Kidder, and S. A. Teukolsky, [arXiv:1004.4697](https://arxiv.org/abs/1004.4697) [*Phys. Rev. D* (to be published)].
- [25] J. A. González, U. Sperhake, B. Brügmann, M. Hannam, and S. Husa, *Phys. Rev. Lett.* **98**, 091101 (2007).
- [26] B. Brügmann, J. A. González, M. Hannam, S. Husa, and U. Sperhake, *Phys. Rev. D* **77**, 124047 (2008).
- [27] P. Jaranowski and G. Schäfer, *Phys. Rev. D* **57**, 7274 (1998).
- [28] T. Damour, P. Jaranowski, and G. Schäfer, *Phys. Lett. B* **513**, 147 (2001).
- [29] T. Damour, P. Jaranowski, and G. Schäfer, *Phys. Rev. D* **62**, 021501 (2000).
- [30] L. Blanchet and G. Faye, *Phys. Rev. D* **63**, 062005 (2001).
- [31] V. C. de Andrade, L. Blanchet, and G. Faye, *Classical Quantum Gravity* **18**, 753 (2001).
- [32] L. Blanchet and B. R. Iyer, *Classical Quantum Gravity* **20**, 755 (2003).
- [33] L. Blanchet, *Classical Quantum Gravity* **15**, 113 (1998).
- [34] L. Blanchet, B. R. Iyer, and B. Joguet, *Phys. Rev. D* **65**, 064005 (2002).
- [35] L. Blanchet, T. Damour, G. Esposito-Farese, and B. R. Iyer, *Phys. Rev. Lett.* **93**, 091101 (2004).
- [36] P. Ajith *et al.*, *Phys. Rev. D* **77**, 104017 (2008).
- [37] M. Campanelli, C. O. Lousto, H. Nakano, and Y. Zlochower, *Phys. Rev. D* **79**, 084010 (2009).
- [38] B. Barker and R. O'Connell, *Phys. Rev. D* **2**, 1428 (1970).
- [39] B. Barker and R. O'Connell, *Gen. Relativ. Gravit.* **5**, 539 (1974).
- [40] B. Barker and R. O'Connell, *Gen. Relativ. Gravit.* **11**, 149 (1979).
- [41] L. E. Kidder, *Phys. Rev. D* **52**, 821 (1995).
- [42] T. Damour, *Phys. Rev. D* **64**, 124013 (2001).
- [43] E. Poisson, *Phys. Rev. D* **57**, 5287 (1998).
- [44] A. Buonanno, Y. Chen, and T. Damour, *Phys. Rev. D* **74**, 104005 (2006).
- [45] G. Faye, L. Blanchet, and A. Buonanno, *Phys. Rev. D* **74**, 104033 (2006).
- [46] L. Blanchet, A. Buonanno, and G. Faye, *Phys. Rev. D* **74**, 104034 (2006).
- [47] T. Damour, P. Jaranowski, and G. Schäfer, *Phys. Rev. D* **77**, 064032 (2008).
- [48] K. Alvi, *Phys. Rev. D* **64**, 104020 (2001).
- [49] H. P. Pfeiffer *et al.*, *Classical Quantum Gravity* **24**, S59 (2007).
- [50] M. Hannam, S. Husa, D. Pollney, B. Brügmann, and N. Ó Murchadha, *Phys. Rev. Lett.* **99**, 241102 (2007).
- [51] M. Hannam *et al.*, *J. Phys. Conf. Ser.* **66**, 012047 (2007).
- [52] M. Hannam, S. Husa, F. Ohme, B. Brügmann, and N. Ó Murchadha, *Phys. Rev. D* **78**, 064020 (2008).
- [53] S. Husa and M. Hannam (2010) (unpublished).
- [54] S. Husa and M. Hannam, in *GR19 meeting, Mexico City, July 2010* (unpublished).
- [55] B. Walther, B. Brügmann, and D. Müller, *Phys. Rev. D* **79**, 124040 (2009).
- [56] P. Ajith *et al.*, [arXiv:0909.2867](https://arxiv.org/abs/0909.2867).
- [57] B. Vaishnav, I. Hinder, F. Herrmann, and D. Shoemaker, *Phys. Rev. D* **76**, 084020 (2007).
- [58] C. Reisswig *et al.*, *Phys. Rev. D* **80**, 124026 (2009).
- [59] K. G. Arun, A. Buonanno, G. Faye, and E. Ochsner, *Phys. Rev. D* **79**, 104023 (2009).
- [60] S. Dain, C. O. Lousto, and Y. Zlochower, *Phys. Rev. D* **78**, 024039 (2008).
- [61] G. Lovelace, R. Owen, H. P. Pfeiffer, and T. Chu, *Phys. Rev. D* **78**, 084017 (2008).
- [62] M. Hannam, S. Husa, and N. Ó Murchadha, *Phys. Rev. D* **80**, 124007 (2009).
- [63] M. Hannam, S. Husa, B. B. Brügmann, J. A. González, and U. Sperhake, *Classical Quantum Gravity* **24**, S15 (2007).
- [64] S. Babak, M. Hannam, S. Husa, and B. F. Schutz, [arXiv:0806.1591](https://arxiv.org/abs/0806.1591).
- [65] P. Ajith, *Classical Quantum Gravity* **25**, 114033 (2008).
- [66] T. Damour, A. Nagar, M. Hannam, S. Husa, and B. Brügmann, *Phys. Rev. D* **78**, 044039 (2008).
- [67] L. Santamaría *et al.*, *Phys. Rev. D* **82**, 064016 (2010).
- [68] M. Boyle *et al.*, *Phys. Rev. D* **76**, 124038 (2007).
- [69] A. Buonanno, G. B. Cook, and F. Pretorius, *Phys. Rev. D* **75**, 124018 (2007).

- [70] J. G. Baker *et al.*, *Phys. Rev. D* **78**, 044046 (2008).
- [71] S. McWilliams (private communication).
- [72] C. Cutler and E. E. Flanagan, *Phys. Rev. D* **49**, 2658 (1994).
- [73] C. Reisswig and D. Pollney, [arXiv:1006.1632](https://arxiv.org/abs/1006.1632).
- [74] T. Damour, B. R. Iyer, and B. S. Sathyaprakash, *Phys. Rev. D* **57**, 885 (1998).
- [75] S. T. McWilliams, B. J. Kelly, and J. G. Baker, *Phys. Rev. D* **82**, 024014 (2010).
- [76] <http://www.lsc-group.phys.uwm.edu/lal>.
- [77] L. Lindblom, B. J. Owen, and D. A. Brown, *Phys. Rev. D* **78**, 124020 (2008).
- [78] <http://www.ninja-project.org/>.
- [79] D. A. Shaddock, *Pub. Astron. Soc. Aust.* **26**, 128 (2009).
- [80] M. Punturo *et al.*, *Classical Quantum Gravity* **27**, 084007 (2010).
- [81] M. Campanelli, C. O. Lousto, and Y. Zlochower, *Phys. Rev. D* **74**, 041501 (2006).
- [82] T. Chu, H. P. Pfeiffer, and M. A. Scheel, *Phys. Rev. D* **80**, 124051 (2009).
- [83] E. Berti, V. Cardoso, and C. M. Will, *Phys. Rev. D* **73**, 064030 (2006).
- [84] P. Marronetti, W. Tichy, B. Brügmann, J. González, and U. Sperhake, *Phys. Rev. D* **77**, 064010 (2008).
- [85] L. Rezzolla *et al.*, *Astrophys. J.* **674**, L29 (2008).
- [86] C. O. Lousto, M. Campanelli, and Y. Zlochower, *Classical Quantum Gravity* **27**, 114006 (2010).
- [87] B. P. Abbott *et al.* (LIGO Scientific Collaboration), *Phys. Rev. D* **80**, 047101 (2009).
- [88] B. P. Abbott *et al.* (LIGO Scientific Collaboration), *Phys. Rev. D* **79**, 122001 (2009).
- [89] A. M. Sintes and A. Vecchio, [arXiv:gr-qc/0005058](https://arxiv.org/abs/gr-qc/0005058).
- [90] C. Van Den Broeck and A. S. Sengupta, *Classical Quantum Gravity* **24**, 1089 (2007).
- [91] J. I. Thorpe *et al.*, *Classical Quantum Gravity* **26**, 094026 (2009).
- [92] S. T. McWilliams, J. I. Thorpe, J. G. Baker, and B. J. Kelly, *Phys. Rev. D* **81**, 064014 (2010).
- [93] M. Alcubierre, *Introduction to 3 + 1 Numerical Relativity* (Oxford University Press, New York, 2008), ISBN .
- [94] E. Berti *et al.*, *Phys. Rev. D* **76**, 064034 (2007).
- [95] J. G. Baker *et al.*, *Astrophys. J.* **653**, L93 (2006).
- [96] F. Herrmann, I. Hinder, D. Shoemaker, and P. Laguna, *Classical Quantum Gravity* **24**, S33 (2007).
- [97] J. G. Baker *et al.*, *Astrophys. J.* **682**, L29 (2008).
- [98] M. Koppitz *et al.*, *Phys. Rev. Lett.* **99**, 041102 (2007).
- [99] D.-I. Choi *et al.*, *Phys. Rev. D* **76**, 104026 (2007).
- [100] M. Campanelli, C. O. Lousto, Y. Zlochower, and D. Merritt, *Astrophys. J.* **659**, L5 (2007).
- [101] J. A. González, M. D. Hannam, U. Sperhake, B. Brügmann, and S. Husa, *Phys. Rev. Lett.* **98**, 231101 (2007).
- [102] M. Campanelli, C. O. Lousto, Y. Zlochower, and D. Merritt, *Phys. Rev. Lett.* **98**, 231102 (2007).
- [103] D. Pollney *et al.*, *Phys. Rev. D* **76**, 124002 (2007).
- [104] C. O. Lousto and Y. Zlochower, *Phys. Rev. D* **77**, 044028 (2008).
- [105] J. Healy *et al.*, *Phys. Rev. Lett.* **102**, 041101 (2009).
- [106] M. Campanelli and C. O. Lousto, *Phys. Rev. D* **59**, 124022 (1999).
- [107] J. G. Baker, J. R. van Meter, S. T. McWilliams, J. Centrella, and B. J. Kelly, *Phys. Rev. Lett.* **99**, 181101 (2007).
- [108] L. E. Kidder, *Phys. Rev. D* **77**, 044016 (2008).
- [109] I. Hinder, F. Herrmann, P. Laguna, and D. Shoemaker, *Phys. Rev. D* **82**, 024033 (2010).
- [110] L. Blanchet, G. Faye, B. R. Iyer, and S. Sinha, *Classical Quantum Gravity* **25**, 165003 (2008).
- [111] D. Brown *et al.*, [arXiv:0709.0093](https://arxiv.org/abs/0709.0093).
- [112] M. Boyle *et al.*, *Phys. Rev. D* **78**, 104020 (2008).
- [113] S. McWilliams, Ph.D. thesis, University of Maryland, 2008.
- [114] C. M. Will and A. G. Wiseman, *Phys. Rev. D* **54**, 4813 (1996).
- [115] E. Berti, V. Cardoso, J. A. Gonzalez, U. Sperhake, and B. Brügmann, *Classical Quantum Gravity* **25**, 114035 (2008).
- [116] M. Boyle (private communication).
- [117] Y. Pan *et al.*, *Phys. Rev. D* **77**, 024014 (2008).
- [118] M. Boyle, D. A. Brown, and L. Pekowsky, *Classical Quantum Gravity* **26**, 114006 (2009).
- [119] M. Hannam, S. Husa, F. Ohme, and P. Ajith, [arXiv:1008.2961](https://arxiv.org/abs/1008.2961).
- [120] D. Christodoulou, *Phys. Rev. Lett.* **25**, 1596 (1970).
- [121] W. Tichy and B. Brügmann, *Phys. Rev. D* **69**, 024006 (2004).